Momentum dependence in K-edge resonant inelastic x-ray scattering and its application to screening dynamics in CE-phase $La_{0.5}Sr_{1.5}MnO_4$

T. F. Seman,[1,*] X. Liu,[2,3] J. P. Hill,[2] M. van Veenendaal,[4,5,†] and K. H. Ahn[1,‡]

[1]*Department of Physics, New Jersey Institute of Technology, Newark, New Jersey 07102, USA*

[2]*Condensed Matter Physics and Materials Science Department, Brookhaven National Laboratory, Upton, New York 11973, USA*

[3]*Beijing National Laboratory for Condensed Matter Physics, and Institute of Physics, Chinese Academy of Sciences, Beijing 100190, China*

[4]*Department of Physics, Northern Illinois University, DeKalb, Illinois 60115, USA*

[5]*Advanced Photon Source, Argonne National Laboratory, Argonne, Illinois 60439, USA*

(Received 2 August 2013; revised manuscript received 9 May 2014; published 9 July 2014)

We present a formula for the calculation of K-edge resonant inelastic x-ray scattering on transition-metal compounds, based on a local interaction between the valence shell electrons and the 1s core hole. Extending a previous result, we include explicit momentum dependence and a basis with multiple core-hole sites. We apply this formula to a single-layered charge-, orbital-, and spin-ordered manganite, $La_{0.5}Sr_{1.5}MnO_4$, and obtain good agreement with experimental data, in particular with regards to the large variation of the intensity with momentum. We find that the screening in $La_{0.5}Sr_{1.5}MnO_4$ is highly localized around the core-hole site and demonstrate the potential of K-edge resonant inelastic x-ray scattering as a probe of screening dynamics in materials.

DOI: 10.1103/PhysRevB.90.045111 PACS number(s): 78.70.Ck, 71.27.+a, 75.47.Lx, 71.10.−w

I. INTRODUCTION

There has been a great interest recently in K-edge resonant inelastic x-ray scattering (RIXS) [1–8], particularly, in transition-metal oxides, because of its unique advantages over other probes. In this spectroscopy, hard x rays with energies of the order of 10 keV excite transition-metal 1s electrons into empty 4p levels, which decay back to the 1s levels. In addition to the elastic process, inelastic processes occur that result in low-energy excitations of the order of 1 eV near the Fermi energy, the cross section of which is enhanced by the resonant condition. The K-edge RIXS spectrum provides information on the momentum dependence of the excitations, is sensitive to the bulk properties because of the high energy of hard x rays and directly probes valance-shell excitations because there is no core hole in the final states. Since early studies on nickel-based compounds [9,10], K-edge RIXS has been a useful probe for novel excitations in transition-metal oxides, in particular, high-T_c cuprates [11,12].

Theoretically, it has been proposed that the K-edge RIXS spectrum reflects different aspects of the electronic structure depending on the size of the core-hole potential, $U_{\rm core}$, between the 1s core hole and the 3d electrons, relative to the 3d band width [8]. In the weak or strong limit of $U_{\rm core}$, the ultrashort core-hole lifetime expansion is applicable [13] and it has been shown that the K-edge RIXS spectrum corresponds to the dynamic structure factor, $S(\mathbf{Q},\omega)$. Some experimental results indeed show K-edge RIXS spectra similar to $S(\mathbf{Q},\omega)$ multiplied by a resonant factor, but others show deviations [14]. In the intermediate case of $U_{\rm core}$, numerical calculations show asymmetric electron-hole excitations and that the RIXS spectrum is substantially modified from $S(\mathbf{Q},\omega)$ [15].

One of the main conclusions of Ref. [15] is that the K-edge RIXS intensity for transition-metal oxides essentially represents the dynamics of electrons near the Fermi energy, which screen the 1s core hole created by the x ray [15,16]. Tuning the incoming x-ray energy to the absorption edge allows an approximation in which the sum over the intermediate states is replaced with the single lowest-energy intermediate state. The study further showed that expanding K-edge RIXS intensity according to the number of final-state electron-hole pairs is a fast-converging expansion where the one-electron-hole-pair states dominate, particularly for insulators. The calculation further shows that the electron excitation is from the unoccupied band throughout entire first Brillouin zone, reflecting the localized nature of the core-hole screening by electrons in real space. In contrast, the hole excitations are mostly from occupied states close to the gap to minimize the kinetic energy, particularly when the gap energy is smaller than the band width.

In Ref. [15], the focus was on the energy dependence of electron-hole excitations and the case of one core-hole site per unit cell. The momentum dependence of the RIXS spectrum and the possibility of multiple core-hole sites within a unit cell were not considered explicitly. In the current paper, we derive a formula that includes the full momentum dependence as well as multiple core-hole sites within a unit cell in the tight-binding approach. The formula is expressed in terms of the intermediate states with a completely localized 1s core hole, and we show that the RIXS spectrum in reciprocal space can be readily compared with the screening cloud in real space.

As a specific example, we calculate the K-edge RIXS spectrum for $La_{0.5}Sr_{1.5}MnO_4$ and make a comparison with experimental results. This material has a layered perovskite structure, which includes two-dimensional MnO_2 planes with eight Mn sites per unit cell in the low-temperature spin-, orbital-, charge-, and structure-ordered state [17–19]. Experimental results show a dramatic variation of the RIXS intensity in reciprocal space in spite of the fact that there is almost no change in the peak energy of the energy-loss feature [20]. We find good agreement between theory and experiment. By

*Current address: Department of Physics, Northern Illinois University, De Kalb, Illinois 60115, USA and Advanced Photon Source, Argonne National Laboratory, Argonne, Illinois 60439, USA.

†veenendaal@niu.edu

‡kenahn@njit.edu

varying the parameter values, we find a correlation between the variation of the K-edge RIXS spectrum in reciprocal space and the size and shape of the screening cloud in real space. We further examine the periodicity of the K-edge RIXS spectrum [21].

The paper is organized as follows. Section II presents the derivation of the K-edge RIXS formula in the limit of a completely localized $1s$ core hole. We present the experimental results and the theoretical model for $La_{0.5}Sr_{1.5}MnO_4$ in Secs. III and IV, respectively. Section V presents calculated K-edge RIXS spectrum, comparison with experimental results, and calculated $S(\mathbf{Q},\omega)$. Section VI includes further discussion on our results and Sec. VII summarizes. Appendix A shows details of the K-edge RIXS formula derivation. Appendix B shows the RIXS formula in terms of eigenstates with and without the core hole. Appendix C includes the expression of the tight-binding Hamiltonian for $La_{0.5}Sr_{1.5}MnO_4$ in reciprocal space. We discuss the actual electron numbers at nominal "Mn^{3+}" and "Mn^{4+}" sites in $La_{0.5}Sr_{1.5}MnO_4$ in Appendix D. The programs used for our calculations are available online [22].

II. K-EDGE RIXS FORMULA IN THE LIMIT OF LOCALIZED 1S CORE HOLE

A. Derivation of the K-edge RIXS formula

The Kramers-Heisenberg formula [8,23] is the starting point for the derivation of our K-edge RIXS formula:

$$I(\omega,\mathbf{k},\mathbf{k}',\boldsymbol{\epsilon},\boldsymbol{\epsilon}') \propto \sum_f \left| \sum_n \frac{\langle f|\mathcal{D}'^{\dagger}|n\rangle\langle n|\mathcal{D}|g\rangle}{E_g+\hbar\omega_{\mathbf{k}}-E_n+i\Gamma_n} \right|^2 \times \delta(E_g-E_f+\hbar\omega), \quad (1)$$

where $|f\rangle$, $|n\rangle$, and $|g\rangle$ represent the final, intermediate, and initial states, E_f, E_n, and E_g are their energies, Γ_n is the inverse of the intermediate state lifetime, $\hbar\omega_{\mathbf{k}}$ is the energy of incoming x-ray with wave vector $\mathbf{k}$, and $\hbar\omega$ is the x-ray energy loss. $\mathcal{D}'^{\dagger}$ and $\mathcal{D}$ are the electric multipole operators, which include the incoming and outgoing x-ray wave vectors and polarization vectors, $(\mathbf{k},\boldsymbol{\epsilon})$ and $(\mathbf{k}',\boldsymbol{\epsilon}')$.

In general, the $1s$ core-hole component of the intermediate eigenstates $|n\rangle$ can be chosen as a delocalized momentum eigenstate [16]. In the limit of the $1s$ electron hopping amplitude approaching zero, the intermediate energy eigenstates with different core hole momenta become degenerate, and the appropriate linear combinations can be made to form intermediate energy eigenstates with a $1s$ core hole completely localized at a chosen site [15,24,25]. Therefore the state $|n\rangle$ can be chosen as $|n^{\mathbf{R}+\mathbf{d}}\rangle$, the intermediate energy eigenstate with the core hole at a site $\mathbf{R}+\mathbf{d}$, where $\mathbf{R}$ and $\mathbf{d}$ represent the lattice point and the relative position of core-hole site within the unit cell, respectively. The summation over intermediate states $\sum_n$ can then be written as three summations, $\sum_{\mathbf{R}}\sum_{\mathbf{d}}\sum_{n^{\mathbf{R}+\mathbf{d}}}$.

We take the dipole approximation [8] for the electric multipole operators $\mathcal{D}'^{\dagger}$ and $\mathcal{D}$. By analyzing how the phases of the intermediate and final eigenstates change following a translation by the lattice vector $\mathbf{R}$, we find that the sum over $\mathbf{R}$ gives rise to conservation of crystal momentum. Under the appropriate experimental conditions, such as for the experiments reported in this paper in which the scattering plane is fixed with respect to the crystal and the incoming x-ray polarization vectors remain perpendicular to the scattering plane as shown in Fig. 1, the polarization effect in the K-edge RIXS is a constant factor. We can then effectively remove the $4p$ creation and annihilation operators and replace the dipole operators by the core-hole creation and annihilation operators. This results in the following expression:

$$I(\omega,\mathbf{k},\mathbf{k}') \propto \sum_{\mathbf{K}}\sum_f \left| \sum_{\mathbf{d}}\sum_{n^{\mathbf{d}}} \frac{e^{-i(\mathbf{k}'-\mathbf{k})\cdot\mathbf{d}}\langle f|\underline{s}_{\mathbf{d}}|n^{\mathbf{d}}\rangle\langle n^{\mathbf{d}}|\underline{s}_{\mathbf{d}}^{\dagger}|g\rangle}{E_g+\hbar\omega_{\mathbf{k}}-E_{n^{\mathbf{d}}}+i\Gamma_{n^{\mathbf{d}}}} \right|^2 \times \delta(E_g-E_f+\hbar\omega)\,\delta(\mathbf{k}_f+\mathbf{k}'-\mathbf{k}+\mathbf{K}), \quad (2)$$

where $\underline{s}_{\mathbf{d}}^{\dagger}$ is the creation operator of the $1s$ core-hole at site $\mathbf{d}$, $\mathbf{K}$ represents a reciprocal lattice vector, and $\mathbf{k}_f$ denotes the net momentum of the final state. Details of the derivation of the above formula are presented in Appendix A.

We make further approximations to simplify the numerical calculation of RIXS spectrum. First, we replace the sum $\sum_{n^{\mathbf{d}}}$ by a single term with $n^{\mathbf{d}}=n^{\mathbf{d}}_{\mathrm{low}}$, that is, the lowest energy eigenstate with the core hole at a site $\mathbf{d}$. This is justified for two reasons [15]. First, $\langle n^{\mathbf{d}}|\underline{s}_{\mathbf{d}}^{\dagger}|g\rangle$ is largest for $n^{\mathbf{d}}_{\mathrm{low}}$, the well-screened state. Second, the incoming x-ray energy is tuned to the absorption edge, which makes the lowest energy intermediate state the most probable, while higher energy intermediate states, in particular, the unscreened state [15], are less likely to be excited by the incoming x-rays in a K-edge RIXS process. The lowest-energy intermediate state $|n^{\mathbf{d}}_{\mathrm{low}}\rangle$ is dominated by the single-pair electron-hole excitations, especially in insulators, because of the higher energies necessary for multiple-pair electron-hole excitations [15]. We therefore consider single-pair final states $\langle l_e\mathbf{k}_e l_h\mathbf{k}_h\sigma|$ with an electron with wave vector $\mathbf{k}_e$, band index l_e, and energy $\varepsilon_{l_e\mathbf{k}_e}$ and a hole with wave vector $\mathbf{k}_h$, band index l_h, and energy $\varepsilon_{l_h\mathbf{k}_h}$, both with spin σ. Finally, if the resonant energies $E_{n^{\mathbf{d}}}-E_g$ and core-hole lifetime broadenings $\Gamma_{n^{\mathbf{d}}}$ are similar for different core-hole sites within the unit cell, then we can neglect the denominator in Eq. (2) for fixed incoming x-ray energy, because it becomes a constant factor in the overall K-edge RIXS spectrum. These approximations lead to the following formula, which we use

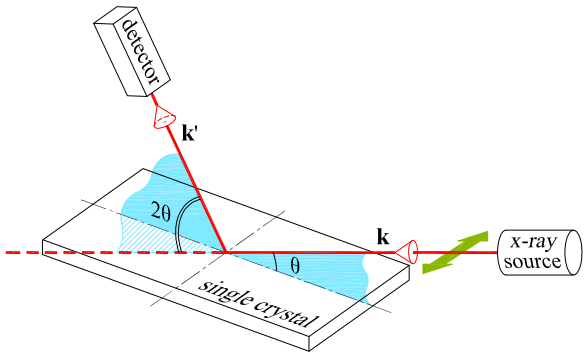

FIG. 1. (Color online) Schematic drawing of the geometry for the K-edge RIXS experiment reported in this paper. The polarization direction is orthogonal to the scattering plane and is depicted with a green arrow.

for the numerical calculation of the K-edge RIXS spectrum:

$$I(\omega,\mathbf{Q}) \propto \sum_{\mathbf{K}} \sum_{l_e\mathbf{k}_e l_h\mathbf{k}_h\sigma} \left| \sum_{\mathbf{d}} e^{-i\mathbf{Q}\cdot\mathbf{d}} \langle l_e\mathbf{k}_e l_h\mathbf{k}_h\sigma | \underline{s}_{\mathbf{d}} | n^{\mathbf{d}}_{\text{low}} \rangle \langle n^{\mathbf{d}}_{\text{low}} | \underline{s}^{\dagger}_{\mathbf{d}} | g \rangle \right|^2 \times \delta(\varepsilon_{l_h\mathbf{k}_h} - \varepsilon_{l_e\mathbf{k}_e} + \hbar\omega)\, \delta(\mathbf{k}_e - \mathbf{k}_h + \mathbf{Q} + \mathbf{K}), \quad (3)$$

where $\mathbf{Q} = \mathbf{k}' - \mathbf{k}$. This formula relates the K-edge RIXS spectrum to the response of the system to a localized charge. The reasonable approximations we have taken significantly reduce the time for numerical calculations, and therefore, this formula can be used with the density functional approach as well as the tight-binding approach. Details on how we numerically calculate $I(\omega,\mathbf{Q})$ with Eq. (3) are presented in Appendix B.

B. Periodicity of K-edge RIXS in reciprocal space

Understanding the periodicity of the K-edge RIXS spectrum is useful, for example, in determining where to probe in reciprocal space. Also, as we will show below, there is useful information in the momentum dependence. First, it should be noted that periodicity in reciprocal space is not inherent in inelastic x-ray scattering. For example, off resonance, an increase in transferred momentum changes the transition matrix elements, since higher-order terms in the multipole expansion of the vector potential $\mathbf{A}$ are no longer negligible [8]. However, on resonance, the matrix elements are all in the dipole limit and should not depend on the momenta of the incoming and outgoing photons. The only relevant momentum is then the crystal momentum, and the K-edge RIXS cross section follows the symmetry of the Brillouin zone. This was noted experimentally by Kim *et al.* [21] in their study of high-T_c cuprates. However, these materials have only one transition metal site in the unit cell. Such periodicity may not be generally applicable to crystals with multiple core-hole sites within a unit cell, such as charge-orbital-ordered manganites.

We look into the formula in Eq. (3) to learn about the periodicity of K-edge RIXS spectrum. For solid systems with one core-hole site per unit cell, we can choose $\mathbf{d} = 0$ and simplify Eq. (3) by omitting a constant factor $\langle n^{\mathbf{d}}_{\text{low}} | \underline{s}^{\dagger}_{\mathbf{d}} | g \rangle$ to obtain

$$I(\omega,\mathbf{Q}) \propto \sum_{\mathbf{K}} \sum_{l_e\mathbf{k}_e l_h\mathbf{k}_h\sigma} \left| \langle l_e\mathbf{k}_e l_h\mathbf{k}_h\sigma | \underline{s}_{\mathbf{d}=0} | n^{\mathbf{d}=0}_{\text{low}} \rangle \right|^2 \times \delta(\varepsilon_{l_h\mathbf{k}_h} - \varepsilon_{l_e\mathbf{k}_e} + \hbar\omega)\, \delta(\mathbf{k}_e - \mathbf{k}_h + \mathbf{Q} + \mathbf{K}), \quad (4)$$

which makes the RIXS calculations even simpler for materials with one core-hole site per unit cell. If the x-ray wave vector change $\mathbf{Q}$ is altered by a reciprocal lattice vector $\mathbf{K}'$, i.e., $\mathbf{Q}' = \mathbf{Q} + \mathbf{K}'$, then the RIXS intensity will be unchanged, since $\mathbf{K}'' = \mathbf{K}' + \mathbf{K}$ in the second δ-function is also a reciprocal lattice vector. This is consistent with the experimental result for La_2CuO_4 (Ref. [21]).

On the other hand, if a solid has multiple core-hole sites per unit cell due to the ordering of spin, charge, orbital, or local lattice distortions, then the following argument shows that the symmetry of the K-edge RIXS spectrum is with respect to the lattice without ordering, rather than the actual lattice. We represent the lattice without ordering by $\mathbf{R}_{\text{core}}$, which includes the actual lattice $\mathbf{R}$ as well as $\mathbf{d}$. Then $\mathbf{K}_{\text{core}}$, the reciprocal lattice vector of $\mathbf{R}_{\text{core}}$, satisfies the condition of $e^{i\mathbf{K}_{\text{core}}\cdot\mathbf{d}} = 1$, which results in the symmetry of K-edge RIXS spectrum in Eq. (3), that is, $I(\omega,\mathbf{Q}+\mathbf{K}_{\text{core}}) = I(\omega,\mathbf{Q})$. We shall see this explicitly in Sec. V F for $La_{0.5}Sr_{1.5}MnO_4$.

III. EXPERIMENTAL RESULTS FOR $La_{0.5}Sr_{1.5}MnO_4$

Mn K-edge RIXS from $La_{0.5}Sr_{1.5}MnO_4$ was measured at the Advanced Photon Source on beamlines 30-ID and 9-ID at temperature $T = 20$ K, well below CE-type magnetic, charge, orbital, and structural ordering temperatures. The instrumental energy resolution was of about 270 meV (FWHM). As shown in Fig. 1, a single crystal grown in traveling solvent floating zone method is aligned so that when the x-ray wave-vector transfer $\mathbf{Q}$ is in the scattering plane, it has $Q_x = Q_y$ with the x and y axes along the Mn-O bond direction and the z axis perpendicular to the MnO_2 plane. The scattering plane was fixed with respect to the crystal and the polarization of the incoming and outgoing x-rays was perpendicular to the scattering plane, so that the polarization factor is a constant factor in the RIXS formula, as assumed in the derivation of Eq. (3). Data taken either at a fixed sample angle, θ, or a fixed detector angle, 2θ, are shown as connected dots in Fig. 2. The elastic peak has been subtracted from the data [20]. The main focus in this paper is the intensity variation of the 2-eV peak, which is known to arise from transitions between Mn $3d$ e_g bands from optical measurements [26,27]. The intensity of the 2-eV peak increases rapidly from $Q_x = Q_y = 0$ to $Q_x = Q_y = \pm\frac{\pi}{a}$, where a represent the average Mn-Mn distance within the MnO_2 plane, but is almost independent of Q_z. The latter supports the two-dimensional character of the e_g electrons confined within each MnO_2 layer. The fact that there are eight core-hole sites per two-dimensional unit cell makes the experimental results for $La_{0.5}Sr_{1.5}MnO_4$ an ideal case to test the validity of our theory.

IV. TIGHT-BINDING HARTREE-FOCK HAMILTONIAN AND CORE-HOLE POTENTIAL FOR e_g ELECTRONS IN $La_{0.5}Sr_{1.5}MnO_4$

$La_{0.5}Sr_{1.5}MnO_4$ has a layered two-dimensional perovskite structure with negligible hopping of the Mn $3d$ e_g electrons between the MnO_2 layers. This is consistent with the experimental observation of K-edge RIXS spectrum being independent of the momentum transfer perpendicular to MnO_2 layers. We therefore consider a Hamiltonian for a single MnO_2 layer. $La_{0.5}Sr_{1.5}MnO_4$ undergoes a structural and orbital ordering transition at 230 K, and a CE-type magnetic ordering transition at 110 K, schematically shown in Fig. 3 for the MnO_2 layer. In this figure, "Mn^{3+}" and "Mn^{4+}" are used to indicate the two sites not related by symmetry, rather than controversial charge ordering [28–30]. The strong Hund's coupling between the e_g electron spin and the t_{2g} electron spin confines most of the e_g electron hopping along the zigzag chain. The distortion of the oxygen octahedron surrounding the Mn ions splits the e_g energy levels through the Jahn-Teller electron-lattice coupling.

Our tight-binding Hamiltonian considers the *effective* Mn $3d$ e_g levels only, because the RIXS peak at around 2 eV is due to transitions between the bands from these levels [26,27].

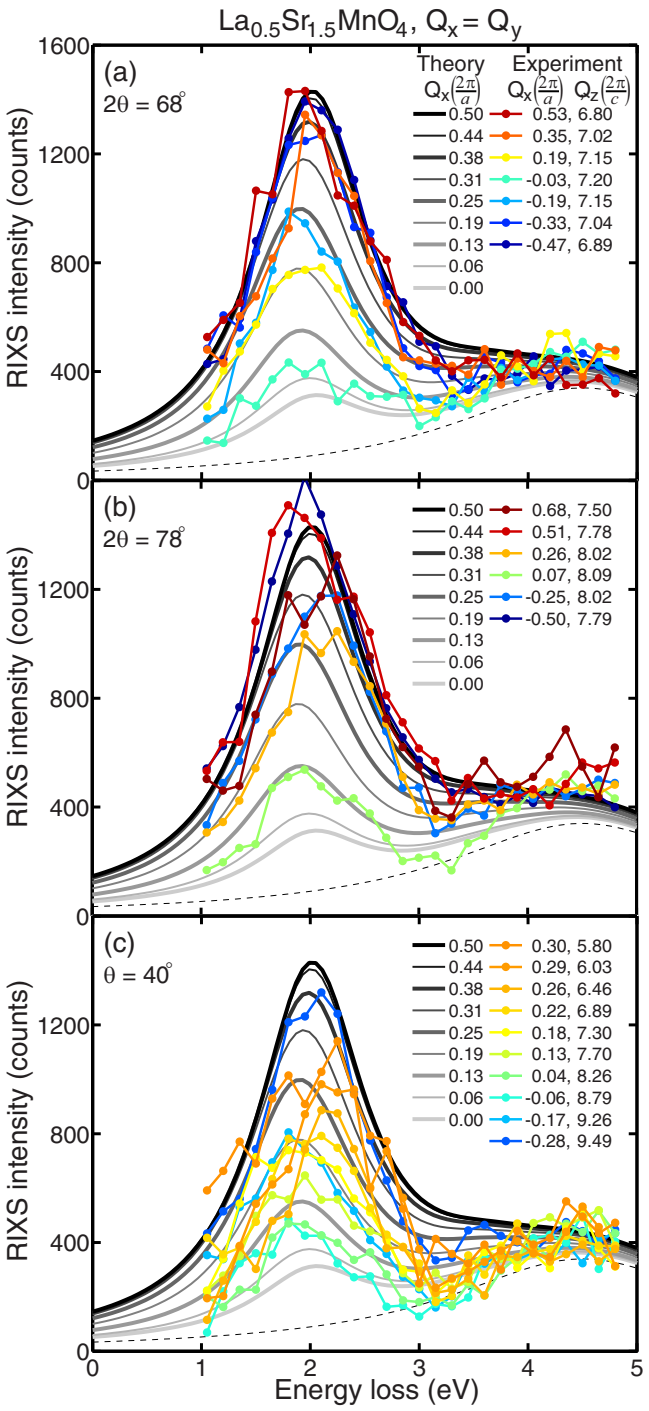

FIG. 2. (Color online) Experimental and theoretical K-edge RIXS intensities for $La_{0.5}Sr_{1.5}MnO_4$ with CE-type charge-orbital-spin ordering. The symbols represent the experimental data, taken at $2\theta = 68^\circ$, $2\theta = 78^\circ$, and $\theta = 40^\circ$, respectively, and $Q_x = Q_y = H_{\rm ex}\frac{2\pi}{a}$ and $Q_z = L_{\rm ex}\frac{2\pi}{c}$ (Ref. [20]). The elastic peaks are subtracted from data [20]. Dashed line represents a momentum-independent peak, presumably from a O-Mn transition. Solid curves in gray scale represent the RIXS intensity calculated at $Q_x = Q_y = H_{\rm th}\frac{2\pi}{a}$ for the Mn-Mn transition for the parameter set with $t_0 = 0.9$ eV, added to the dashed line, as discussed in Sec. V D.

We note that these effective Mn $3d$ e_g levels are in fact linear combinations of *atomic* Mn $3d$ e_g levels and *atomic* O $2p$

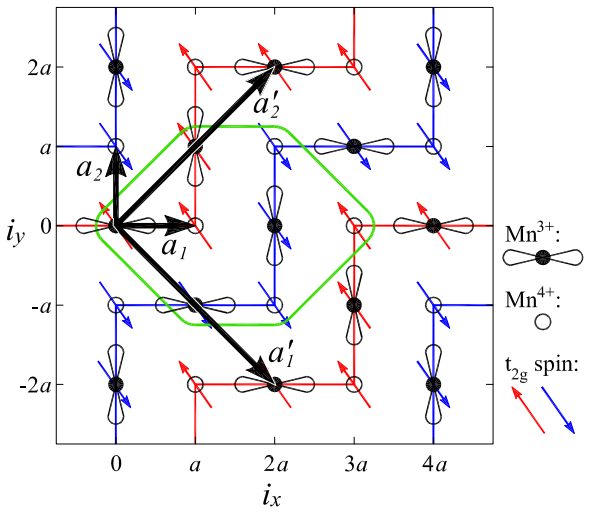

FIG. 3. (Color online) In-plane structural layout of Mn ions for $La_{0.5}Sr_{1.5}MnO_4$ in CE-type ordering. Red and blue arrows represent the t_{2g} spin alignment. $\mathbf{a}_1'$ and $\mathbf{a}_2'$ represent the primitive lattice vectors for CE phase. $\mathbf{a}_1$ and $\mathbf{a}_2$ are primitive vectors for lattice without charge, orbital, and spin ordering. The rounded hexagon encloses the Mn ions in the basis.

levels. Appendix D discusses this aspect in more detail, in particular, in relation to the electron numbers on the Mn ions.

Within this effective model, we define $d^\dagger_{\mathbf{i}\xi\sigma}$ as the creation operator of the e_g electron with the spin state $\sigma = \uparrow, \downarrow$ and orbital state $\xi = 1$ for $(3z^2 - r^2)/2$ and $\xi = 2$ for $\sqrt{3}(x^2 - y^2)/2$ at the Mn site $\mathbf{i} = (m_x a, m_y a)$, where m_x and m_y are integers, as shown in Fig. 3. The electron hopping term [31] is

$$\hat{H}_{\rm hopping} = -\frac{1}{2}\sum_{\mathbf{i},\boldsymbol{\delta},\xi,\xi',\sigma} t^{\xi\xi'}_{\boldsymbol{\delta}}\left(d^\dagger_{\mathbf{i}\xi\sigma}d_{\mathbf{i}+\boldsymbol{\delta},\xi',\sigma} + d^\dagger_{\mathbf{i}+\boldsymbol{\delta},\xi',\sigma}d_{\mathbf{i}\xi\sigma}\right). \quad (5)$$

The vector $\boldsymbol{\delta} = \pm a\hat{x}, \pm a\hat{y}$ represents the nearest-neighbor sites of a Mn ion. The hopping matrices within the MnO_2 plane are

$$t_{a\hat{x}} = t_{-a\hat{x}} = t_0\begin{pmatrix} 1/4 & -\sqrt{3}/4 \\ -\sqrt{3}/4 & 3/4 \end{pmatrix}, \quad (6)$$

$$t_{a\hat{y}} = t_{-a\hat{y}} = t_0\begin{pmatrix} 1/4 & \sqrt{3}/4 \\ \sqrt{3}/4 & 3/4 \end{pmatrix}, \quad (7)$$

reflecting the symmetry of the e_g orbitals. The parameter t_0 represents the effective hopping constant between the two $(3x^2 - r^2)/2$ orbitals along the x direction.

The distortion of oxygen octahedron around a Mn ion at site $\mathbf{i}$ is parameterized as follows. $u^\zeta_{\mathbf{i}}$ $(\zeta = x, y)$ represents the $\hat{\zeta}$ directional displacement of an oxygen ion located between Mn ions at $\mathbf{i}$ and $\mathbf{i} + a\hat{\zeta}$ from the position for the ideal undistorted square MnO_2 lattice with the average in-plane Mn-O bond distance. The $u^{+z}_{\mathbf{i}}$ and $u^{-z}_{\mathbf{i}}$ represent the z direction displacements of the oxygen ions above and below the Mn ion at site $\mathbf{i}$ from the location of the average in-plane Mn-O bond distance. The parameters, $Q_{1\mathbf{i}}$, $Q_{2\mathbf{i}}$, and $Q_{3\mathbf{i}}$, represent the distortion modes of the oxygen octahedron, shown in Fig. 4

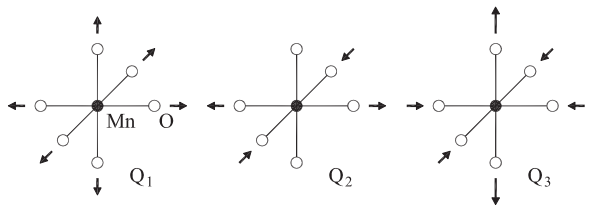

FIG. 4. Distortion modes Q_1, Q_2, and Q_3 of oxygen octahedron around Mn with arrows indicating directions of displacement.

and defined as follows:

$$Q_{1\mathbf{i}} = \frac{u^x_{\mathbf{i}} - u^x_{\mathbf{i}-a\hat{x}} + u^y_{\mathbf{i}} - u^y_{\mathbf{i}-a\hat{y}} + u^{+z}_{\mathbf{i}} - u^{-z}_{\mathbf{i}}}{\sqrt{3}}, \tag{8}$$

$$Q_{2\mathbf{i}} = \frac{u^x_{\mathbf{i}} - u^x_{\mathbf{i}-a\hat{x}} - u^y_{\mathbf{i}} + u^y_{\mathbf{i}-a\hat{y}}}{\sqrt{2}}, \tag{9}$$

$$Q_{3\mathbf{i}} = \frac{2u^z_{\mathbf{i}} - 2u^{-z}_{\mathbf{i}} - u^x_{\mathbf{i}} + u^x_{\mathbf{i}-a\hat{x}} - u^y_{\mathbf{i}} + u^y_{\mathbf{i}-a\hat{y}}}{\sqrt{6}}. \tag{10}$$

The Mn-O bond distances estimated from structural refinement of high-resolution synchrotron x-ray powder diffraction data for $La_{0.5}Sr_{1.5}MnO_4$ in Ref. [32] indicate $Q_1 = 0.0531$ Å, $Q_2 = \pm 0.1089$ Å, and $Q_3 = 0.0955$ Å around the "Mn^{3+}" sites and $Q_1 = -0.0531$ Å, $Q_2 = 0$, and $Q_3 = 0.1192$ Å around the "Mn^{4+}" sites.

The Q_2 and Q_3 distortions break the cubic symmetry of the oxygen octahedra and interact with the e_g orbital state through the following Jahn-Teller Hamiltonian term [33]:

$$\hat{H}_{\mathrm{JT}} = -\lambda \sum_{\mathbf{i},\sigma} \begin{pmatrix} d^\dagger_{\mathbf{i}1\sigma} \\ d^\dagger_{\mathbf{i}2\sigma} \end{pmatrix}^T \begin{pmatrix} Q_{3\mathbf{i}} & -Q_{2\mathbf{i}} \\ -Q_{2\mathbf{i}} & -Q_{3\mathbf{i}} \end{pmatrix} \begin{pmatrix} d_{\mathbf{i}1\sigma} \\ d_{\mathbf{i}2\sigma} \end{pmatrix}, \tag{11}$$

where λ corresponds to the Jahn-Teller coupling constant. The isotropic Q_1 distortion interacts with the total e_g electron number through the following "breathing" electron-lattice Hamiltonian term [34]:

$$\hat{H}_{\mathrm{br}} = -\beta\lambda \sum_{\mathbf{i},\sigma} \begin{pmatrix} d^\dagger_{\mathbf{i}1\sigma} \\ d^\dagger_{\mathbf{i}2\sigma} \end{pmatrix}^T \begin{pmatrix} Q_{1\mathbf{i}} & 0 \\ 0 & Q_{1\mathbf{i}} \end{pmatrix} \begin{pmatrix} d_{\mathbf{i}1\sigma} \\ d_{\mathbf{i}2\sigma} \end{pmatrix}, \tag{12}$$

where β represents the ratio between the strengths of the breathing and the Jahn-Teller coupling.

We also include the Hund's coupling of the e_g electron spin state to the classical t_{2g} spin direction,

$$\hat{H}_{\mathrm{Hund}} = -J_H \sum_{\mathbf{i},\xi,\sigma',\sigma''} \mathbf{S}_{t_{2g}\mathbf{i}} \cdot d^\dagger_{\mathbf{i}\xi\sigma'} \boldsymbol{\tau}_{\sigma'\sigma''} d_{\mathbf{i}\xi\sigma''}, \tag{13}$$

where J_H represents the Hund's coupling constant, $\mathbf{S}_{t_{2g}\mathbf{i}}$ the t_{2g} spin vector ordered in CE-type structure and $\boldsymbol{\tau}$ is the Pauli matrix vector.

As in Ref. [31], we also include the $3d$-$3d$ on-site Coulomb interaction,

$$\hat{H}_{\mathrm{dd}} = U \sum_{\mathbf{i}} \sum_{(\eta,\sigma)\neq(\eta',\sigma')} \hat{n}_{\mathbf{i}\eta\sigma} \hat{n}_{\mathbf{i}\eta'\sigma'}, \tag{14}$$

where $\hat{n}_{\mathbf{i}\eta\sigma} = d^\dagger_{\mathbf{i}\eta\sigma} d_{\mathbf{i}\eta\sigma}$ is the number operator and U represents the size of the $3d$-$3d$ Coulomb interaction. The index $\eta = -,+$ represents the local orbital eigenstates of $\hat{H}_{\mathrm{JT}}$ with lower and higher energies, respectively, chosen for the following Hartree-Fock approximation:

$$\hat{H}^{\mathrm{HF}}_{\mathrm{dd}} = \sum_{\mathbf{i}} (U_{\mathbf{i}+\uparrow} d^\dagger_{\mathbf{i}+\uparrow} d_{\mathbf{i}+\uparrow} + U_{\mathbf{i}-\uparrow} d^\dagger_{\mathbf{i}-\uparrow} d_{\mathbf{i}-\uparrow} + U_{\mathbf{i}+\downarrow} d^\dagger_{\mathbf{i}+\downarrow} d_{\mathbf{i}+\downarrow} + U_{\mathbf{i}-\downarrow} d^\dagger_{\mathbf{i}-\downarrow} d_{\mathbf{i}-\downarrow}), \tag{15}$$

where $U_{\mathbf{i}+\uparrow} = U(\langle \hat{n}_{\mathbf{i}-\uparrow} \rangle + \langle \hat{n}_{\mathbf{i}+\downarrow} \rangle + \langle \hat{n}_{\mathbf{i}-\downarrow} \rangle)$, etc. [31].

The total Hamiltonian for Mn $3d$ e_g electrons for calculations of K-edge RIXS initial and final states is then the sum of the terms described so far,

$$\hat{H}_{\mathrm{d}} = \hat{H}_{\mathrm{hopping}} + \hat{H}_{\mathrm{JT}} + \hat{H}_{\mathrm{br}} + \hat{H}_{\mathrm{Hund}} + \hat{H}^{\mathrm{HF}}_{\mathrm{dd}}. \tag{16}$$

The CE-type ordering of the t_{2g} spins and the lattice distortions associated with charge and orbital ordering give rise to the primitive lattice vectors $\mathbf{a}'_1$ and $\mathbf{a}'_2$ shown in Fig. 3. The primitive reciprocal lattice vectors are $\mathbf{b}'_1 = (\frac{\pi}{2a}, -\frac{\pi}{2a})$ and $\mathbf{b}'_2 = (\frac{\pi}{2a}, \frac{\pi}{2a})$, and the first Brillouin zone is $\Omega_{1\mathrm{BZ}} = \{\mathbf{k} | -\frac{\pi}{2a} < k_x + k_y \leqslant \frac{\pi}{2a}, -\frac{\pi}{2a} < k_x - k_y \leqslant \frac{\pi}{2a}\}$.

In the intermediate state, we must also account for the presence of the core hole. The $1s$-$3d$ on-site Coulomb interaction is generally expressed as

$$\hat{H}_{\mathrm{sd}} = -U_{\mathrm{core}} \sum_{\mathbf{i},\xi,\sigma,\sigma'} d^\dagger_{\mathbf{i}\xi\sigma} d_{\mathbf{i}\xi\sigma} \underline{s}^\dagger_{\mathbf{i}\sigma'} \underline{s}_{\mathbf{i}\sigma'}, \tag{17}$$

where U_{core} represents the size of the $1s$-$3d$ Coulomb interaction, and $\underline{s}^\dagger_{\mathbf{i}\sigma'}$ is the creation operator for a $1s$ core hole with spin σ' at site $\mathbf{i}$. As discussed in Sec. II A, in the limit of vanishing $1s$ electron hopping amplitude, the K-edge RIXS intermediate energy eigenstates can be chosen as states with a single completely localized $1s$ core hole, which can be found from

$$\hat{H}_{\mathrm{total},\mathbf{i}_c} = \hat{H}_{\mathrm{d}} + \hat{H}_{\mathrm{sd},\mathbf{i}_c}, \tag{18}$$

with

$$\hat{H}_{\mathrm{sd},\mathbf{i}_c} = -U_{\mathrm{core}} \sum_{\xi,\sigma} d^\dagger_{\mathbf{i}_c\xi\sigma} d_{\mathbf{i}_c\xi\sigma}, \tag{19}$$

$\mathbf{i}_c$ representing the $1s$ core-hole site, and $\underline{s}^\dagger_{\mathbf{i}_c\sigma'} \underline{s}_{\mathbf{i}_c\sigma'} = 1$ being used. To calculate the K-edge RIXS spectrum, we need to represent the eigenstates of $\hat{H}_{\mathrm{total},\mathbf{i}_c}$, as a linear combination of the eigenstates of $\hat{H}_{\mathrm{d}}$, as described in detail in Appendix B. The expression of the Hamiltonian $\hat{H}_{\mathrm{d}}$ and $\hat{H}_{\mathrm{total},\mathbf{i}_c}$ in reciprocal space for $La_{0.5}Sr_{1.5}MnO_4$ is presented in Appendix C.

Each Hamiltonian term has one parameter. Some of the parameter values are chosen by modifying corresponding values for $LaMnO_3$ found in Ref. [31]. The chosen parameter values are $t_0 = 0.9$ eV, $\lambda = 7.41$ eV/Å, $\beta = 1.5$, $J_H|\mathbf{S}_{t_{2g},\mathbf{i}}| = 2.2$ eV, $U = 3.5$ eV, and $U_{\mathrm{core}} = 4.0$ eV. In addition, we vary t_0 and λ while maintaining the gap size around 2 eV to examine how the RIXS spectrum depends on the e_g electron hopping amplitude.

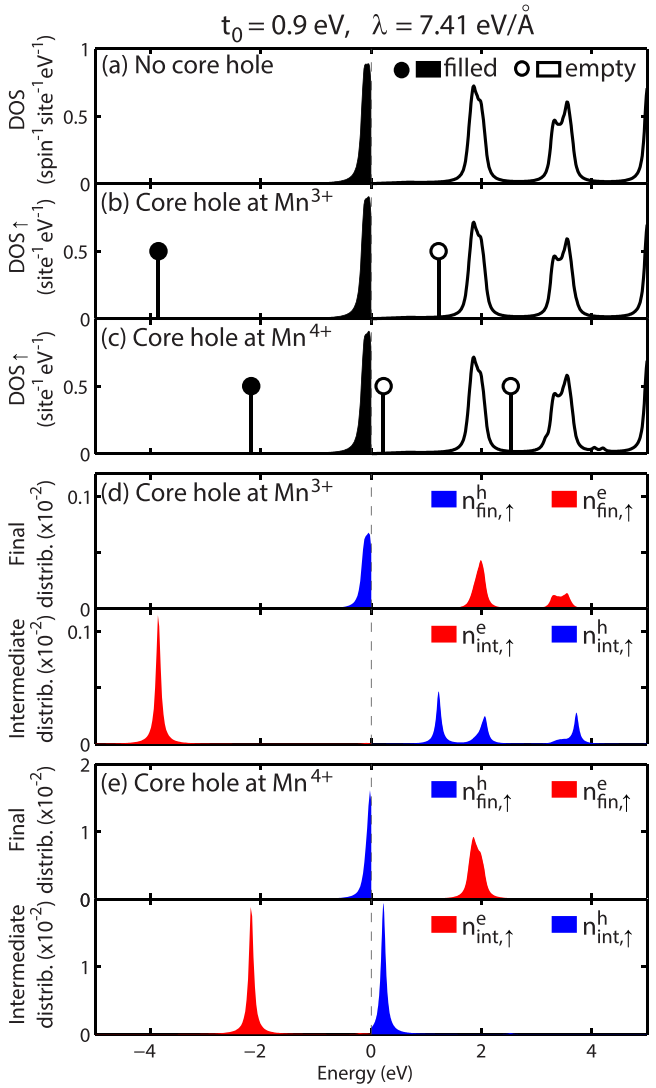

FIG. 5. (Color online) Electronic density of states (DOS) per site, for $t_0 = 0.9$ eV and $\lambda = 7.41$ eV/Å (a) without a core hole, (b) with a core hole at a Mn^{3+} site and (c) with a core hole at a Mn^{4+} site. The Lorentzian broadening of $2\Gamma = 0.1$ eV is used to make the DOS curve smooth. Vertical lines with a circle on top represent bound states. (d) and (e) Final (upper panel) and intermediate (lower panel) electron-hole distribution with a core hole at a (d) Mn^{3+} and (e) Mn^{4+} site.

V. RESULTS FROM THEORY AND COMPARISON WITH EXPERIMENTS

A. Electronic density of states in the absence and in the presence of the core hole

We first present our results on energy eigenstates and eigenvalues of the Hamiltonians for a 16×16 Mn site cluster with periodic boundary conditions. The calculated density of states (DOS) is shown in Fig. 5(a) in the absence of a core hole. The occupied band mostly consists of the lower Jahn-Teller e_g levels with spin parallel to the t_{2g} spins at Mn^{3+} sites, whereas the lowest empty band mostly consists of similar e_g levels at Mn^{4+} sites. The excitation between these two bands is responsible for the 2 eV RIXS peak, which is the focus of our comparison with experiment data. Due to spin degeneracy in CE-type antiferromagnetic ordering, the electronic DOS $D_\downarrow(\varepsilon)$ for spin ↓, is identical to that for spin ↑, $D_\uparrow(\varepsilon)$.

We next analyze the Hamiltonian $\hat{H}_{\text{total},\mathbf{i}_c}$ in the presence of the core hole at site $\mathbf{i}_c$. The t_{2g} spin direction at $\mathbf{i}_c$ breaks the spin degeneracy in the DOS. The DOS $D_\uparrow^{\mathbf{i}_c=(0,0)}(\varepsilon)$ is displayed in Fig. 5(b), for the core hole site $\mathbf{i}_c = (0,0)$ in Fig. 3, which is a Mn^{3+} site with t_{2g} spin ↑. The core-hole potential pulls out bound states from the band continuum [15], identified by vertical lines with circles on top in Fig. 5(b). The lowest bound state is at about −4 eV, that is, U_{core} below the lowest band with Mn^{3+} character. The second bound state is within the gap. The DOS for the band continuum is almost unchanged, except that the number of states within each band below and above the gap is reduced by one because of the bound states pulled out [15]. By filling the states from the lowest energy with the same number of electrons in the intermediate states as in the ground state, as shown in Fig. 5(b), we obtain the lowest energy intermediate state, $\underline{s}|n_{\text{low}}^{\mathbf{i}_c}\rangle$. Therefore the bound state below the lowest band is occupied and the bound state within the gap is empty in the intermediate state. $D_\downarrow^{\mathbf{i}_c=(0,0)}(\varepsilon)$ is almost identical to the DOS without a core hole in Fig. 5(a), because the electrons with spin ↓ contribute very little to the screening of the core hole due to the strong Hund's coupling.

The DOS $D_\uparrow^{\mathbf{i}_c=(a,0)}(\varepsilon)$, for the core hole at $\mathbf{i}_c = (a,0)$ in Fig. 3, which is a Mn^{4+} site with t_{2g} spin ↑, is shown in Fig. 5(c) and has similar features. The lowest bound state is at around −2 eV, that is, U_{core} below the band with the Mn^{4+} site character, which is the lowest empty band. Again, the lowest bound state is filled and the bound state within the gap is empty for $\underline{s}|n_{\text{low}}^{\mathbf{i}_c}\rangle$, as indicated in Fig. 5(c).

As a comparison, we carry out similar calculations for the parameter values of $t_0 = 1.5$ eV and $\lambda = 3.51$ eV/Å, which keep the size of the gap approximately 2 eV, but result in a larger band width. Due to the larger electron hopping, the gap has more of a hybridization gap character, and the bands are wider, as shown in Fig. 6(a), which shows the DOS without a core hole. Similarly to the $t_0 = 0.9$ eV case, Figs. 6(b) and 6(c) show $D_\uparrow^{\mathbf{i}_c}(\varepsilon)$, in the presence of a core hole at $\mathbf{i}_c = (0,0)$ and $\mathbf{i}_c = (a,0)$, respectively. The bound states in Fig. 6(c) are qualitatively similar to those for $t_0 = 0.9$ eV in Fig. 5(c). However, qualitatively different behavior occurs for the core hole at a Mn^{3+} site, as shown in Fig. 6(b). In this case, the bound state that would be in the gap for smaller t_0 resides in the occupied band and becomes a resonant rather than bound state, as indicated by the vertical line with "R" on top. Such a resonant state hybridizes with delocalized states in the band, unlike bound states. With the bound state below the lower band and this resonant state occupied, the top of the lower band is empty in the lowest energy intermediate state $\underline{s}|n_{\text{low}}^{\mathbf{i}_c}\rangle$, as indicated in Fig. 6(b). This will have a significant consequence in the screening dynamics, as discussed in following sections.

B. Electron and hole excitations by the core hole represented along energy axis

Understanding the distributions of the electrons and holes that are excited by the core hole is essential for the interpretation of RIXS spectrum. Excited electron and hole distributions

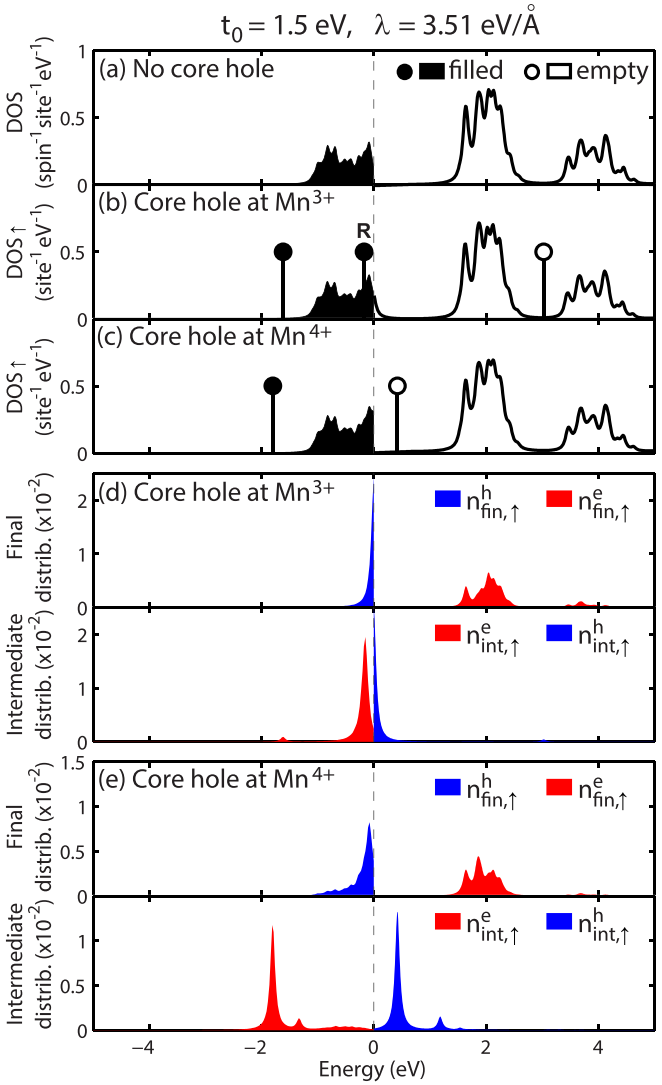

FIG. 6. (Color online) Similar figures as Fig. 5 for $t_0 = 1.5$ eV and $\lambda = 3.51$ eV/Å. "R" in (b) represents a resonant state, rather than a bound state. Note that a single state at the top of the lower band in (b) is empty.

with respect to the energy for the RIXS *final* state, $n^e_{\mathrm{fin},\sigma}(\varepsilon)$ with $\varepsilon > \varepsilon_F$ and $n^h_{\mathrm{fin},\sigma}(\varepsilon)$ with $\varepsilon < \varepsilon_F$, are defined as follows [15]:

$$n^e_{\mathrm{fin},\sigma}(\varepsilon) = \sum_{l\mathbf{k}}^{\varepsilon_{l\mathbf{k}\sigma}>\varepsilon_F} \sum_{m=1}^{\frac{N_e}{2}} |\langle 0|b_{l\mathbf{k}\sigma} c^\dagger_{m\sigma}|0\rangle|^2 \delta(\varepsilon - \varepsilon_{l\mathbf{k}\sigma}), \quad (20)$$

$$n^h_{\mathrm{fin},\sigma}(\varepsilon) = \sum_{l\mathbf{k}}^{\varepsilon_{l\mathbf{k}\sigma}<\varepsilon_F} \sum_{m=\frac{N_e}{2}+1}^{} |\langle 0|b_{l\mathbf{k}\sigma} c^\dagger_{m\sigma}|0\rangle|^2 \delta(\varepsilon - \varepsilon_{l\mathbf{k}\sigma}), \quad (21)$$

where ε_F represents the Fermi energy in the absence of the core hole, $c^\dagger_{m\sigma}$ is the creation operator for the mth lowest energy eigenstate of $\hat{H}_{\mathrm{total},\mathbf{i}_c}$ with spin σ and energy $\varepsilon_{m\sigma}$, and $b^\dagger_{l\mathbf{k}\sigma}$ represents the creation operator for the energy eigenstate with wave vector $\mathbf{k}$ and energy $\varepsilon_{l\mathbf{k}\sigma}$ within the lth lowest band of $\hat{H}_{\mathrm{d}}$, and N_e represents total electron number. These are the electrons and holes that are moved by the scattering process. For example, $n^e_{\mathrm{fin}}(\varepsilon)$ corresponds to the projection of occupied intermediate states to unoccupied initial states. The δ function makes this distribution represented with respect to the energy without the core hole.

Similar electron and hole distributions with respect to the energy for the RIXS *intermediate* state [15], $n^e_{\mathrm{int},\sigma}(\varepsilon)$ and $n^h_{\mathrm{int},\sigma}(\varepsilon)$, are defined in the same way as Eqs. (20) and (21), except that the energy δ function is replaced by $\delta(\varepsilon - \varepsilon_{m\sigma})$. This difference also implies that we have $n^e_{\mathrm{int},\sigma}(\varepsilon)$ for $\varepsilon < \varepsilon_F^{\mathrm{int}}$ and $n^h_{\mathrm{int},\sigma}(\varepsilon)$ for $\varepsilon > \varepsilon_F^{\mathrm{int}}$, where $\varepsilon_F^{\mathrm{int}}$ represents the Fermi energy in the presence of the core hole.

These excited electron and hole distributions are plotted in Figs. 5(d), 5(e), 6(d), and 6(e) for $\sigma = \uparrow$. Similar distributions for spin $\downarrow$ state are less than 10% of those for spin $\uparrow$ state. The plots of $n^e_{\mathrm{int},\uparrow}(\varepsilon)$ and $n^h_{\mathrm{int},\uparrow}(\varepsilon)$ in the *lower* panels of Figs. 5(d), 5(e), and 6(e) show that the bound states in the intermediate state, marked in Figs. 5(b), 5(c), and 6(c), respectively, make the dominant contribution to the electron-hole excitations.

The plots of $n^h_{\mathrm{fin},\uparrow}(\varepsilon)$ and $n^e_{\mathrm{fin},\uparrow}(\varepsilon)$ in the *upper* panels of Figs. 5(d), 5(e), and 6(e), show that, while $n^e_{\mathrm{fin},\sigma}(\varepsilon)$ resembles the DOS of the unoccupied band, $n^h_{\mathrm{fin},\sigma}(\varepsilon)$ shows a peak at the top of the occupied band, in particular, in Fig. 6(e). This represents asymmetric screening dynamics between electrons and holes.

For the exceptional case of $t_0 = 1.5$ eV and a core hole at Mn^{3+} site, the comparison between Fig. 6(b) and the lower panel in Fig. 6(d) reveals that the occupied resonant state within the lower band marked by "R" and the empty state at the top of the occupied band in Fig. 6(b) make dominant contributions to $n^e_{\mathrm{int},\uparrow}(\varepsilon)$ and $n^h_{\mathrm{int},\uparrow}(\varepsilon)$. The resonant state is dominant for electron excitations because this state is pulled from the initially unoccupied bands, whereas the lowest bound state comes mostly from the initially occupied band. The delocalized state at the top of the occupied band predominantly contributes to the hole excitation, because it is occupied in the initial state and empty in the intermediate state, which results in hole excitation very close to the gap shown in the upper panel in Fig. 6(d). We note that these results are consistent with the conclusions of Ref. [15], thus validating the present study.

C. Electron and hole excitations by the core hole represented in real space

In this section, we present the distribution of electrons and holes excited by the core hole in real space.

First, in the absence of the core hole, the electron number $\langle \hat{n}_{\mathbf{i}\eta\sigma} \rangle$ is calculated for each spin state $\sigma = \uparrow, \downarrow$ and orbital state $\eta = +, -$ at each site $\mathbf{i}$ from the initial ground state $|g\rangle$ of the Hamiltonian $\hat{H}_{\mathrm{d}}$. The total e_g electron numbers calculated for our 16×16 cluster in the absence of the core hole are 0.87 at the nominal Mn^{3+} site and 0.13 at the nominal Mn^{4+} site for the parameter set with $t_0 = 0.9$ eV, indicating a difference of 0.74 in charge density between these two sites. We note that these numbers should not be directly compared with the local density approximation theory results or resonant x-ray scattering results, because our effective Mn $3d$ e_g states are not pure atomic Mn orbital states but combinations of atomic Mn and O orbitals [35]. A proper comparison is described in Appendix D, which shows that the electron numbers in

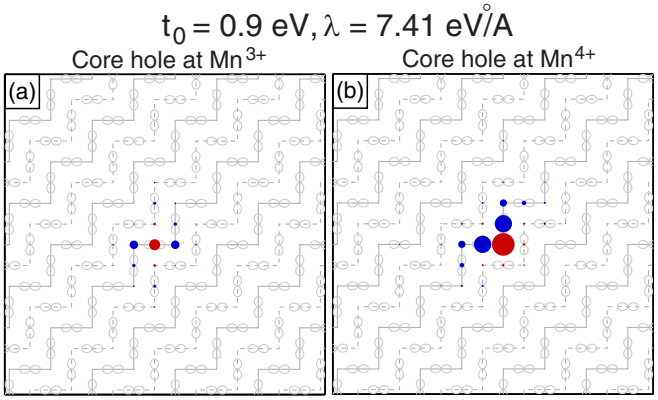

FIG. 7. (Color online) Screening configuration in real space for $t_0 = 0.9$ eV with a core hole at (a) Mn^{3+} and (b) Mn^{4+} sites. The volume of the red and blue spheres is proportional to the excited electron and hole numbers, respectively. The excited electron number at the core-hole site (the site with the largest red sphere) is 0.11 for (a) and 0.92 for (b).

our model are consistent with local density approximation and resonant x-ray scattering results. It is found that most of these electrons occupy the lower Jahn-Teller level $\eta = -$, approximately $\sqrt{3}(x^2 - z^2)/2$ or $\sqrt{3}(y^2 - z^2)/2$ orbital at the Mn^{3+} site and the $(3z^2 - r^2)/2$ orbital at the Mn^{4+} site, with spin parallel to t_{2g} spin at each site, consistent with the orbital ordering proposed in Ref. [36].

In the intermediate state, these electron numbers change to screen the core hole. The changes in electron number, that is, excited electron and hole numbers, are shown in Fig. 7 for $t_0 = 0.9$ eV and in Fig. 8 for $t_0 = 1.5$ eV, where the volumes of red and blue spheres are proportional to the excited electron and hole numbers, respectively. Note that these changes in electron and hole numbers are consistent with the excited electron and hole distributions along the energy axis reported in Figs. 5(d), 5(e), 6(d), and 6(e). The site with the largest electron number in each panel corresponds to the core-hole site. The gray solid and dashed lines in the background represent the zigzag chain with t_{2g} spin ↑ and ↓, respectively. For the

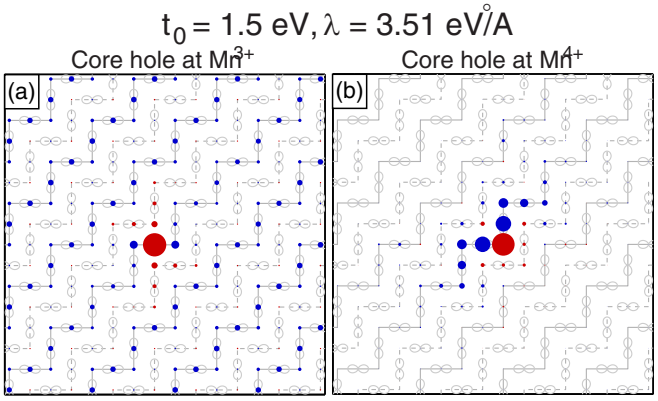

FIG. 8. (Color online) Screening configuration in real space for $t_0 = 1.5$ eV with a core hole at (a) Mn^{3+} and (b) Mn^{4+} sites, similar to Fig. 7. The excited electron number at the core-hole site is 1.02 for (a) and 0.91 for (b) [37].

$t_0 = 0.9$ eV case, Figs. 7(a) and 7(b) show that the excited electrons are mostly confined right at the core-hole site. The localization of the electrons in the intermediate state leads to the relatively broad electron distribution, $n^e_{\mathrm{fin}\uparrow}(\varepsilon)$, along the energy axis in the upper panels of Figs. 5(d) and 5(e). Comparison of the largest solid red spheres in Figs. 7(a) and 7(b) shows that more screening electrons accumulate at the core-hole site when the core hole is created at the Mn^{4+} site (0.92 electron) than at the Mn^{3+} (0.11 electron). This result can be understood from the orbital ordering pattern: initially, the Mn^{4+} site has less e_g electrons on the site itself but more electrons at its nearest neighbor Mn sites along the zigzag chain with orbitals pointing toward the Mn^{4+} site compared to the Mn^{3+} site, which allows the core hole at Mn^{4+} sites to attract more electrons. Hole distribution in Figs. 7(a) and 7(b) show that these screening electrons are mostly from the nearest neighbors along the zigzag chain, accounting for about 90% of the total hole number. The results show that even though the hole excitation is not as localized as the electron excitation and $n^h_{\mathrm{fin}\uparrow}(\varepsilon)$ is sharper along the energy axis than $n^e_{\mathrm{fin}\uparrow}(\varepsilon)$ in Figs. 5(d) and 5(e), the holes are still tightly bound to the core-hole site forming an excitonlike electron-hole-pair state.

The situation changes for the case of large electron hopping $t_0 = 1.5$ eV. Figure 8(a) shows the electron-hole excitations for a core hole at a Mn^{3+} site. In this case, the hole distribution becomes delocalized, and only about 8% of the hole is localized within the nearest neighbors of the core-hole site, while the majority of the hole is delocalized along the zigzag chains with the same spin direction as the core-hole site, consistent with the result in Figs. 6(b) and 6(d). The hole number does not decay with the distance from the core-hole site, indicating qualitatively different screening dynamics. Even for the case with a core hole at a Mn^{4+} site, Fig. 8(b), the hole distribution spreads to further neighbors along the zigzag chain, reflecting the tendency toward delocalization. As we shall see, such screening patterns in real space can be related to the variation of the RIXS intensity in reciprocal space. This will be discussed in Sec. V E.

D. Calculated *K*-edge RIXS spectrum and comparison with experimental data

We calculate the RIXS intensity, $I(\omega,\mathbf{Q})$ according to Eq. (3). To make a comparison between the calculated results and the experimental data, we first examine the experimental data more closely. In addition to the momentum-dependent RIXS peak at around 2 eV, the experimental RIXS spectrum in Fig. 2 shows momentum-independent spectral weight, in particular, above 3 eV. The shape of the experimental RIXS spectrum, particularly with small in-plane wave vector changes, such as $Q_x = Q_y = -0.03 \times \frac{2\pi}{a}$ in Fig. 2(a), indicates that the RIXS spectral weight above 3 eV may have the same origin as the 4–5 eV O $2p$-Mn $3d$ transition observed in optical experiments in related manganites [27]. Based on this assumption, we model the experimental RIXS spectrum with a momentum-independent peak, shown in dashed lines in Fig. 2, centered at 4.5 eV and with a half width at half maximum of 1.5 eV similar to the optical peak, and a momentum-dependent Mn $3d$-$3d$ peak around 2 eV, calculated from Eq. (3) using $\hat{H}_{\mathrm{d}}$ and $\hat{H}_{\mathrm{total},\mathbf{i}_c}$. Here and for the rest of the paper, although it does

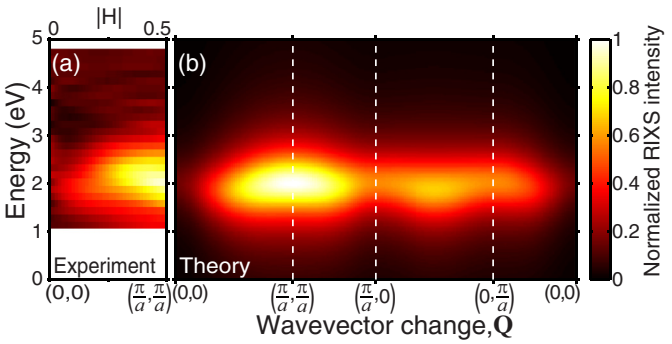

FIG. 9. (Color online) (a) Experimental RIXS intensity. Here we take experimental data of Fig. 2, subtract the 4.5-eV peak, and fit the resulting data with a fifth-order polynomial, which is plotted as a contour plot. (b) Contour plot of the calculated RIXS intensity for the $t_0 = 0.9$ eV case along the chosen path in reciprocal space. We apply the Lorentzian broadening of $2\Gamma = 1.2$ eV along the energy axis and polynomial fits along the path in reciprocal space.

not affect the results much, we present the RIXS intensity averaged over twin domains in the crystal with zigzag chains along the [110] and [$\bar{1}$10] directions, $I_{\rm avg}(\omega,(Q_x,Q_y)) = [I(\omega,(Q_x,Q_y)) + I(\omega,(-Q_x,Q_y))]/2$. The results in Fig. 2 demonstrate a reasonable agreement between the calculated spectra shown in solid lines and the experimental data shown in symbols, considering the experimental noise. The 4.5-eV peak has a substantial tail even in the range of 1–3 eV. Such momentum-independent tails have also been observed in bilayer manganites [38].

To compare just the 2-eV peak between the theory and experiment, we subtract the 4.5-eV peak from the experimental data and plot the intensity, as a contour plot in the plane of energy and $Q_x = Q_y = H_{\rm ex}\frac{2\pi}{a}$ in Fig. 9(a). This clearly shows the momentum dependence of the intensity of the 2-eV peak. The calculated RIXS intensity in Fig. 9(b) for $t_0 = 0.9$ eV shows good agreement with experimental data. In contrast, in Fig. 10, we show the calculated RIXS spectrum for $t_0 = 1.5$ eV, which is not consistent with the experimental data.

E. Energy-integrated RIXS intensity in reciprocal space

To make a more quantitative comparison between theory and experiment, we integrate the spectrum of the 2-eV peak

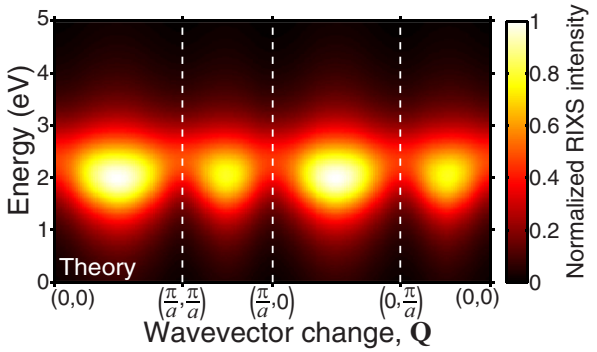

FIG. 10. (Color online) Contour plot of the calculated RIXS intensity for $t_0 = 1.5$ eV along the chosen path in reciprocal space.

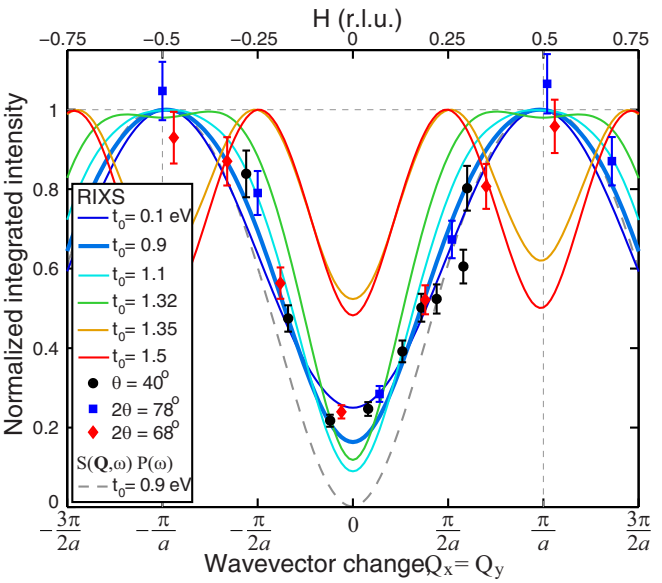

FIG. 11. (Color online) Solid lines and symbols with error bars represent the K-edge RIXS intensity, integrated from 1 to 3 eV and normalized to the maximum, as a function of wave-vector change. The solid lines are from the theory for several t_0 cases for comparison, while the symbols are from the experiments. Dashed gray line represents $S(\mathbf{Q},\omega)P(\omega)$, the dynamic structure factor times a resonant factor, for $t_0 = 0.9$ eV, integrated from 1 to 3 eV and normalized with respect to the maximum, which vanishes completely at $\mathbf{Q} = (0, 0)$ unlike theoretical and experimental integrated RIXS intensity. See Sec. IV E for the comparison between the theoretical and experimental integrated RIXS intensity, and Sec. IV g for comparison between the RIXS intensity and the dynamic structure factor.

from 1 to 3 eV after subtracting 4.5-eV peak, for both theory and experiment. The results are shown in Fig. 11 along the diagonal direction in reciprocal space, in which the theoretical results for the various parameter sets, and the experimental data are normalized with respect to the maximum integrated intensity. The parameter sets used for the calculations are $(t_0,\lambda) = (0.1$ eV, 10.79 eV/Å), (0.9 eV, 7.41 eV/Å), (1.1 eV, 4.81 eV/Å), (1.32 eV, 3.76 eV/Å), (1.35 eV, 3.73 eV/Å), and (1.50 eV, 3.51 eV/Å), chosen to keep the peak at around 2 eV. All other parameter values are unchanged. The experimental data in Fig. 11 shows that the integrated RIXS intensity increases 4–5 times as the wave vector $\mathbf{Q}$ varies from $\mathbf{Q} = (0,0)$ to $\mathbf{Q} = (\frac{\pi}{a},\frac{\pi}{a})$. Considering fluctuations in experimental data, the theoretical results for $t_0 = 0.1, 0.9, 1.1$ eV, all of which have excitonlike screening electron-hole excitations similar to Fig. 7, fit the experimental data reasonably well. In contrast, the theoretical results for $t_0 = 1.35$ and 1.5 eV, all of which have delocalized hole excitations similar to Fig. 8, are qualitatively different from experimental data with maximum intensity at around $(\pm\frac{\pi}{2a}, \pm\frac{\pi}{2a})$ instead of $(\pm\frac{\pi}{a}, \pm\frac{\pi}{a})$. This provides an upper limit of about 1.2 eV for the value of t_0.

This analysis indicates that, irrespective of the details of the model Hamiltonian and the particular parameter values, the rapid increase of the RIXS intensity with a maximum at $(\pm\frac{\pi}{a}, \pm\frac{\pi}{a})$ observed in the experiment is indicative of highly localized screening dynamics [39] in $La_{0.5}Sr_{1.5}MnO_4$, i.e., screening that is more like Fig. 7 than that of Fig. 8.

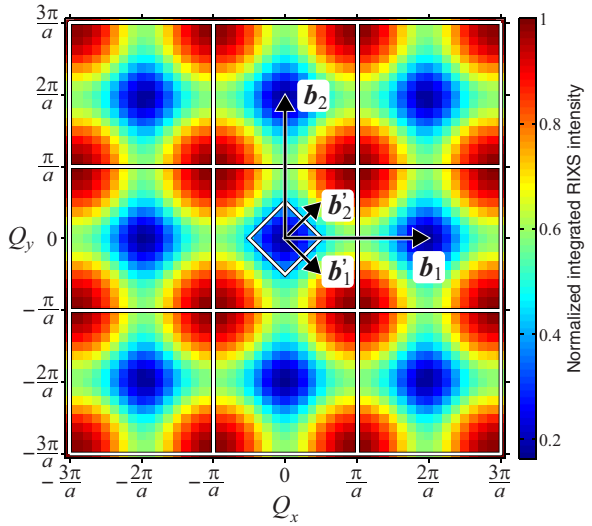

FIG. 12. (Color online) K-edge RIXS intensity integrated from 1 to 3 eV, shown in a large reciprocal space for the $t_0 = 0.9$ eV case. $\mathbf{b}_1'$ and $\mathbf{b}_2'$ represent the primitive reciprocal lattice vectors of charge-orbital-spin-ordered MnO_2 plane of Fig. 3. $\mathbf{b}_1$ and $\mathbf{b}_2$ are the primitive reciprocal lattice vectors for MnO_2 lattice without ordering.

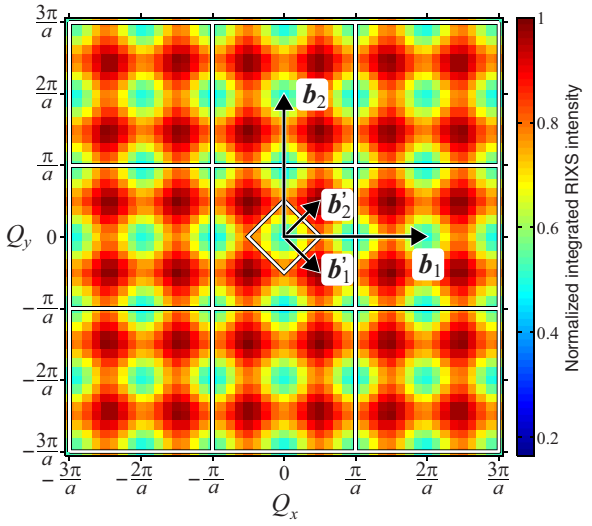

FIG. 13. (Color online) Similar figure as Fig. 12 for the $t_0 = 1.5$ eV case.

F. Periodicity of K-edge RIXS spectrum in reciprocal space for charge-orbital-spin-ordered manganites

As mentioned in Sec. II B, in earlier studies of La_2CuO_4, it was shown that the observed K-edge RIXS spectrum reflects the periodicity of the lattice and is a function of the reduced wave vector $\mathbf{q}$ within the first Brillouin zone, defined as $\mathbf{Q} = \mathbf{q} + \mathbf{K}$, where $\mathbf{Q}$ is the total x-ray wave-vector change and $\mathbf{K}$ is a reciprocal lattice vector [21].

The experimental data presented in this paper clearly indicate that such periodicity is not present for $La_{0.5}Sr_{1.5}MnO_4$. The measured RIXS intensity, as well as the calculated RIXS intensity, seen in Figs. 9 and 11, increases continuously past the boundary of the first Brillouin zone at $(\frac{\pi}{4a}, \frac{\pi}{4a})$. As discussed in Sec. II B, the periodicity seen in Ref. [21] applies only to solids with one core-hole site per unit cell, such as La_2CuO_4. For solids with multiple core-hole sites per unit cell due to the ordering of spin, charge, orbital, or local lattice distortions, the periodicity in K-edge RIXS spectrum follows the periodicity of the lattice without ordering, like the square Mn-site lattice in $La_{0.5}Sr_{1.5}MnO_4$, not the periodicity of the actual lattice with ordering. Our numerical calculations in Figs. 12 and 13 confirm such periodicity in $La_{0.5}Sr_{1.5}MnO_4$: Fig. 12 shows energy-integrated RIXS intensity calculated for the $t_0 = 0.9$ eV case in a larger region of reciprocal space of $-\frac{3\pi}{a} < Q_x \leqslant \frac{3\pi}{a}$ and $-\frac{3\pi}{a} < Q_y \leqslant \frac{3\pi}{a}$. The diamond around (0,0) is the actual first Brillouin zone of the spin, charge, and orbital-ordered structure, whereas the outer square domain $-\frac{\pi}{a} < Q_x \leqslant \frac{\pi}{a}$ and $-\frac{\pi}{a} < Q_y \leqslant \frac{\pi}{a}$, denotes the first Brillouin zone of the lattice without ordering. It is evident that RIXS spectrum does not exhibit periodicity with respect to the actual primitive reciprocal lattice vectors, $\mathbf{b}_1'$ and $\mathbf{b}_2'$, shown in Fig. 12, but rather shows periodicity with respect to primitive reciprocal lattice vectors of the lattice without ordering, $\mathbf{b}_1$ and $\mathbf{b}_2$, shown in Fig. 12. Even though it is only a single data point, the experimental data at around $Q_x = Q_y = 0.68 \times \frac{2\pi}{a}$ in Fig. 11 is consistent with such periodicity. Further experimental data for $|Q_x| > \frac{\pi}{a}$, $|Q_y| > \frac{\pi}{a}$ are required for the verification of this periodicity. We note that careful examination of Fig. 12 reveals that the periodicity is only approximate. The small displacement of the Mn^{4+} ions of 0.0265 Å along the diagonal direction from the ideal square lattice [36], included in our calculations, makes the Mn sites deviate slightly from the exact square lattice. Figure 13 shows that, even for the $t_0 = 1.5$ eV case, the periodicity still does not follow the actual reciprocal lattice, even though the RIXS intensity oscillates more rapidly in reciprocal space [40].

We next provide a physical explanation of why the K-edge RIXS spectrum from charge-orbital-ordered manganites follows the periodicity of the Brillouin zone in the absence of charge-orbital order. We first consider *artificial* doubling of the unit cell for a one-dimensional chain with interatomic distance a. In Fig. 14, thick (blue) lines, both solid and dashed, and solid lines, both thick (blue) and thin (red), show a schematic diagram of the band structure before and after the artificial unit cell doubling, respectively. The arrows between $1s$ and $4p$ bands represent the core hole creation and annihilation by x rays. Due to the interaction with the core-hole, electron-hole pairs can be excited into the valence shell, as indicated by the arrows within the $3d$ band. Excitations with a transferred crystal wave vector $\mathbf{Q}$ from the state 1 can be either an intraband transition to the state 2 shown in Fig. 14(a) or an interband transition to the state 3 shown in Fig. 14(b). However, the reduced Brillouin zone $[-\frac{\pi}{2a}, \frac{\pi}{2a}]$ is an artificial construction and should give equivalent results to the real Brillouin zone $[-\frac{\pi}{a}, \frac{\pi}{a}]$, in which the state $3'$ in Fig. 14(b) should be considered instead of the state 3. Therefore, the intraband and interband transitions correspond to wave-vector transfers of $\mathbf{Q}$ and $\mathbf{Q} + \mathbf{K}$, respectively, where $\mathbf{K}$ is $-\frac{\pi}{a}$, a reciprocal lattice vector of the doubled unit cell. This implies that they occur at two distinct wave-vector transfers and should be distinguishable. The underlying reason is that not only the valence bands are backfolded due to the doubling of unit

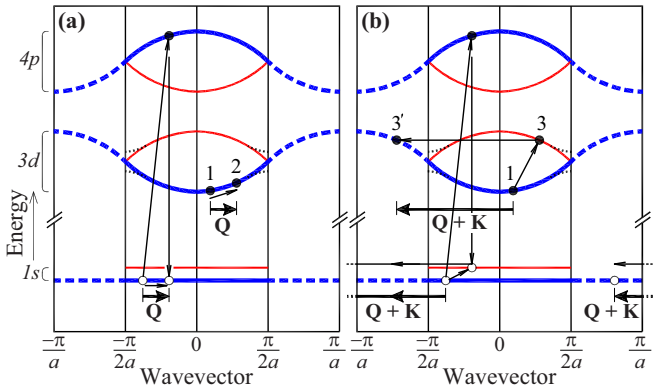

FIG. 14. (Color online) Schematic diagrams of a band structure of a one-dimensional system with a lattice constant a, before [thick (blue) lines, both solid and dashed] and after [solid lines, both thick (blue) and thin (red)] *artificial* unit cell doubling. The thin black dotted lines in the $3d$ bands represent the modification of the band structure after *real* unit cell doubling due to charge-orbital ordering. (a) and (b) represent the RIXS processes that result in x-ray wave-vector transfers of $\mathbf{Q}$ and $\mathbf{Q}+\mathbf{K}$, respectively, with $\mathbf{K}=-\frac{\pi}{a}$, a reciprocal lattice vector for the lattice with the doubled unit cell.

cell, but also the core level bands. An interband (intraband) transition in the valence band also leads to an interband (intraband) transition in the core level band, as shown in arrows in the $1s$ band in Fig. 14. We now consider *real* unit cell doubling due to charge-orbital order. For a finite but small charge-orbital order, the band structure would be modified mostly near the Brillouin zone boundary, as represented by the thin black dotted lines in the $3d$ bands in Fig. 14, and the RIXS that involves states far from the zone boundary, such as the states 1, 2, and 3, should not dramatically change from those in the absence of charge-orbital order. Therefore the K-edge RIXS spectrum $I(\omega,\mathbf{Q})$ and $I(\omega,\mathbf{Q}+\mathbf{K})$ would remain different even after charge-orbital ordering. Obviously, the situation becomes more complex when the charge-orbital order becomes stronger leading to a further mixing of the bands. However, the schematic figure explains why the periodicity for charge-orbital-ordered manganites occurs with the Brillouin zone in the absence of such order.

G. Comparison with dynamic structure factor $S(\mathbf{Q},\omega)$

In this section, we present the dynamic structure factor $S(\mathbf{Q},\omega)$ multiplied by a resonant factor for the CE-phase $La_{0.5}Sr_{1.5}MnO_4$, and compare it with the K-edge RIXS spectrum. Dynamic structure factor can be written as follows for crystals with multiatom bases [41]:

$$S(\mathbf{Q},\omega)=\sum_{\sigma,l,l',\mathbf{k}}\left|M^{ll'\sigma}_{\mathbf{Qk}}\right|^2\delta(\omega-\varepsilon_{l',\mathbf{k}+\mathbf{Q}}+\varepsilon_{l\mathbf{k}}), \quad (22)$$

where

$$M^{ll'\sigma}_{\mathbf{Qk}}=\sum_{\mathbf{d},\xi}\langle\mathbf{k}+\mathbf{Q},l'\sigma|d^{\dagger}_{\mathbf{k}+\mathbf{Q},\mathbf{d}\xi\sigma}d_{\mathbf{kd}\xi\sigma}|\mathbf{k}l\sigma\rangle e^{i\mathbf{Q}\cdot\mathbf{d}}, \quad (23)$$

where l and l' are indices for occupied and unoccupied bands, $\mathbf{k}$ is a vector within the first Brillouin zone, $d_{\mathbf{kd}\xi\sigma}$ is the Fourier transform of $d_{\mathbf{Rd}\xi\sigma}$, that is, the annihilation operator for the

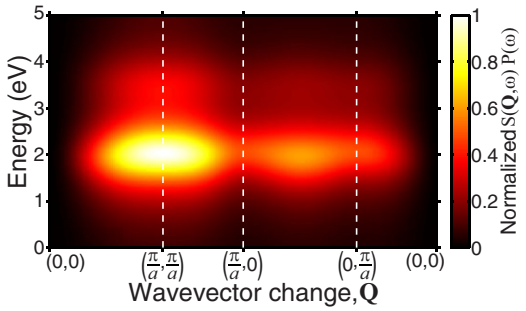

FIG. 15. (Color online) Contour plot of the calculated $S(\mathbf{Q},\omega)P(\omega)$ for $t_0=0.9$ eV along the chosen path in reciprocal space. $S(\mathbf{Q},\omega)P(\omega)$ vanishes completely at $\mathbf{Q}=(0,0)$, unlike theoretical and experimental RIXS intensity shown in Fig. 9.

electron in the orbital state ξ and spin state σ at the site $\mathbf{d}$ within the unit cell at $\mathbf{R}$, and $|\mathbf{k}l\sigma\rangle$ represents an eigenstate with spin σ and energy $\varepsilon_{l\mathbf{k}}$. The resonant factor with the incoming photon energy fixed at the resonance can be written as [13]

$$P(\omega)=C\frac{1}{\omega^2+\Gamma^2}, \quad (24)$$

where Γ represents the inverse of the intermediate state lifetime, chosen approximately as 1 eV, and C is a factor independent of $\mathbf{Q}$ and ω.

The dynamic structure factor $S(\mathbf{Q},\omega)$ calculated for $La_{0.5}Sr_{1.5}MnO_4$ for the parameter set with $t_0=0.9$ eV, multiplied by the resonant factor $P(\omega)$, is shown in Fig. 15, along the same path chosen for Fig. 9. Even though it affects the results only slightly, the average over twin domains has been applied to Fig. 15, as done for the RIXS spectrum. Comparison between Figs. 9 and 15 shows a qualitative similarity, that is, the growth of the intensity from $\mathbf{Q}=0$ to $\mathbf{Q}=(\frac{\pi}{a},\frac{\pi}{a})$. However, a close examination reveals that $S(\mathbf{Q},\omega)P(\omega)$ intensity at $\mathbf{Q}=0$ vanishes completely, consistent with the general property of $S(\mathbf{Q}=0,\omega)=0$ [41], while the experimental and theoretical K-edge RIXS intensity remains finite at $\mathbf{Q}=0$, about 20 % of the maximum. This difference near $\mathbf{Q}=0$ is clearly seen in the integrated $S(\mathbf{Q},\omega)P(\omega)$ between 1 and 3 eV, normalized with respect to $\mathbf{Q}=(\frac{\pi}{a},\frac{\pi}{a})$, shown in dashed gray line in Fig. 11. We also find that $S(\mathbf{Q},\omega)$ is approximately periodic with respect to $\mathbf{b_1}$ and $\mathbf{b_2}$, the primitive reciprocal lattice vectors for MnO_2 lattice without ordering, similar to the periodicity in the K-edge RIXS spectrum shown in Fig. 12.

Qualitative similarity between K-edge RIXS and $S(\mathbf{Q},\omega)P(\omega)$ breaks down for $t_0=1.5$ eV case, for which normalized $S(\mathbf{Q},\omega)P(\omega)$ increases rapidly from zero at $\mathbf{Q}=0$ up to the maximum around $\mathbf{Q}=(\frac{\pi}{2a},\frac{\pi}{2a})$ and decreases by about 10 % towards $\mathbf{Q}=(\frac{\pi}{a},\frac{\pi}{a})$, unlike the calculated K-edge RIXS spectrum in Figs. 10 and 11. This breakdown is consistent with the results in Ref. [15], in which it was demonstrated for a simple model that the energy dependence of the K-edge RIXS spectrum deviates substantially from the dynamic factor $S(\omega)$ as the band width becomes comparable to or larger than the gap size. The above comparison shows both usefulness and limitation of the dynamic structure factor $S(\mathbf{Q},\omega)$ in interpreting the K-edge RIXS spectrum, particularly in the momentum dependence.

VI. DISCUSSION

In this section, we discuss what insights the RIXS spectrum in reciprocal space can provide on the screening dynamics. Figures 16(a) and 16(b) show $n_h/n_h^{\max}$, that is, the hole density normalized to its maximum, versus distance l from the core-hole site along the zigzag chain for the case of core hole at a Mn^{3+} and Mn^{4+} site, respectively, in a semilogarithmic plot. For $t_0 \leqslant 1.3$ eV of Fig. 16(a) and all t_0 of Fig. 16(b), the hole density decreases exponentially and thus can be fit to $n_h/n_h^{\max} \propto \exp(-l/l_s)$, where l_s can be interpreted as the size of the screening cloud. We find that the sizes of the screening clouds are approximately 0.4 and 0.5 interatomic distances for the Mn^{3+} and Mn^{4+} sites, respectively, for $t_0 = 0.9$ eV, and become larger, as t_0 increases, as shown along the horizontal axis in Fig. 16(c), which includes the result for $t_0 = 0.6$ eV additionally.

We next look for a correlation between the size of the screening cloud in real space and the features of the K-edge RIXS spectrum in reciprocal space. We define γ_H as the half width at half maximum in reciprocal space of the energy-integrated RIXS peak for $t_0 \leqslant 1.3$ eV in Fig. 11. The plot of γ_H versus l_s is displayed in Fig. 16(c), which shows a linear correlation. Therefore, the width of the energy-integrated RIXS peak in reciprocal space in Fig. 11 can be used to estimate the size of the screening hole cloud. This correlation is an important result with general implications, and is inherently rooted in the K-edge RIXS process, which involves the projection of the intermediate screening state onto final electron-hole excitations.

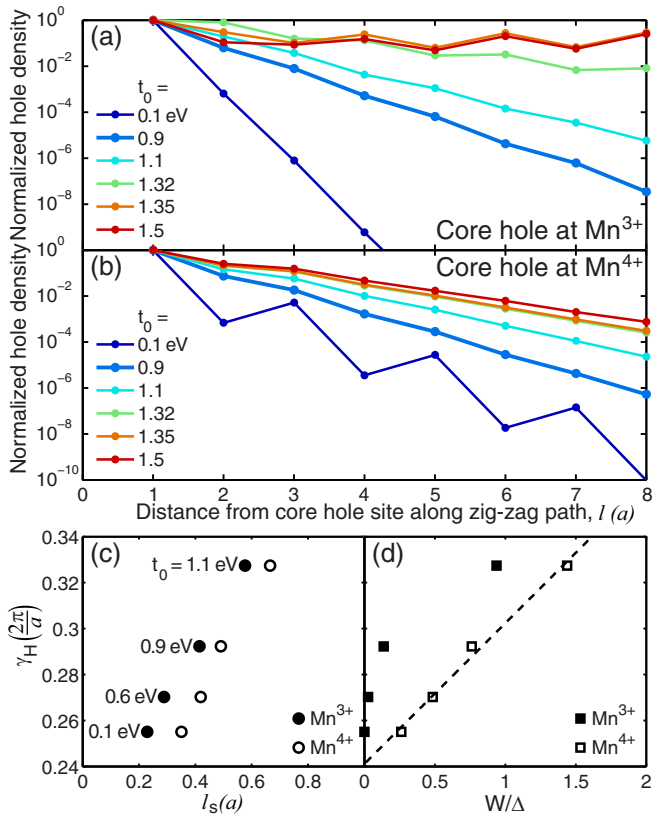

FIG. 16. (Color online) (a) and (b) Semilogarithmic plot of the excited hole number normalized to its maximum versus the distance from the core-hole site for a Mn^{3+}, and a Mn^{4+} core hole site, respectively. (c) The width of the RIXS peak at $(\pm\frac{\pi}{a}, \pm\frac{\pi}{a})$ in reciprocal space, γ_H, found from Fig. 11, vs screening cloud size in real space l_s, found from (a) and (b), for various t_0 values. (d) γ_H vs the ratio between the occupied band width (W) and the in-gap bound state energy (Δ) from the occupied band edge, W/Δ.

The size of the screening hole cloud depends on the competition between hole hopping and hole binding energies, which can be parameterized in terms of W, the width of the occupied band, and Δ, the energy difference between the top of the occupied band and the unoccupied bound state within the gap, or, the hole binding energy. Therefore, from the connection between l_s and γ_H established above, we examine whether the width of the RIXS peak γ_H can also provide insight on the ratio W/Δ. The γ_H versus W/Δ plot in Fig. 16(d) confirms a positive correlation between these quantities, in particular a linear correlation for the case of core hole at Mn^{4+} site. The results indicate that the width of the RIXS peak can be a measure of the size of the excitonlike screening cloud in real space, and a measure of the ratio between the occupied band width and the hole binding energy.

Recently, K-edge RIXS spectra for bilayer manganites $La_{2-2x}Sr_{1+2x}Mn_2O_7$ with $x = 0.36$ and 0.5 have been reported by Weber *et al.* [38]. Although not as pronounced as our results for single layered manganites, Ref. [38] shows an increase of the 2-eV peak intensity in A-type and CE-type antiferromagnetic $LaSr_2Mn_2O_7$, as the x-ray wave-vector transfer increases from $(0,0,Q_z)$ to $(\frac{\pi}{a},\frac{\pi}{a},Q_z)$. In the context of our work above, such results can be interpreted as the formation of an excitonlike screening cloud in bilayer manganites, the size of which is likely larger than that for the single-layer manganites discussed above, considering the less-pronounced increase of the 2-eV peak intensity.

Finally, we note that Semba *et al.* calculated the K-edge RIXS spectrum for $LaMnO_3$, based on the Keldysh-type Green's function formalism [16]. The results in Ref. [16] show about a 10% increase of the 2-eV peak from (0,0,0) to (1,0,0) in their choice of x and y axes, which are equivalent to $\mathbf{Q} = (0,0,0)$ to $\mathbf{Q} = (\frac{\pi}{a},\frac{\pi}{a},0)$ in our notation. The results again can be interpreted as the formation of excitonlike screening clouds, consistent with our calculations, even though the core-hole state for the intermediate eigenstates is chosen as delocalised in Ref. [16]. The periodicity of the RIXS spectrum discussed in Secs. II B and V F was also identified in Ref. [16], even though the association of such periodicity with the approximate square lattice of the core-hole sites was not specifically mentioned.

VII. SUMMARY

We have presented a formalism to calculate the K-edge RIXS spectra in transition metal oxides based on tight-binding Hamiltonians and a local $1s$–$3d$ Coulomb interaction, in which the choice of intermediate eigenstates with a completely localized $1s$ core hole allows for the interpretation of the data in terms of screening dynamics in real space. We have also found that the periodicity of K-edge RIXS spectrum follows the reciprocal lattice vectors of the lattice without the ordering of spin, charge, orbital, or local lattice distortions, rather than the reciprocal lattice vectors of the actual lattice with such ordering.

We have applied our formalism to the highly-momentum-dependent K-edge RIXS spectrum observed for $La_{0.5}Sr_{1.5}MnO_4$ in CE-type spin-orbital-structure ordering. It is found that the sharp increase of the 2-eV peak intensity from the center toward the corner of the first Brillouin zone of the lattice without ordering is an indication of a highly localized screening cloud in $La_{0.5}Sr_{1.5}MnO_4$ with a typical size of 0.4–0.5 Mn-Mn distances. We also showed that there exists a positive correlation between the width of the energy-integrated K-edge RIXS intensity peak in reciprocal space, the size of the excitonlike screening cloud in real space, and the ratio between occupied bandwidth and hole binding energy.

The analysis in this paper was performed for the case of an intermediate strength core-hole potential, that is $U_{\rm core}$ comparable to the $3d$ electron bandwidth. In fact, this is appropriate for most transition metal oxides and therefore the present approach should have general applicability. One of the important results is that this approach highlights the connection between K-edge RIXS and the impurity problem in strongly correlated electron systems, and we show that this technique is a new probe of momentum-dependent screening dynamics of localized impurities. The dynamics of the screening is important information embedded in K-edge RIXS spectrum.

ACKNOWLEDGMENTS

We thank D. Casa, D. Prabhakaran, A. T. Boothroyd, and H. Ding for their invaluable support in experiments. We also thank B. Barbiellini, R. S. Markiewicz, and A. Bansil for useful discussions during CMCSN Workshops. The collaborations between T.F.S., K.H.A., and M.v.V. were supported by the Computational Materials and Chemical Science Network under Grants Nos. DE-FG02-08ER46540 and DE-SC0007091. K.H.A. was further supported by 2012 and 2013 Argonne X-ray Science Division Visitor Program. M.v.V. was supported by the US Department of Energy, Office of Basic Energy Sciences, Division of Materials Sciences and Engineering under Award No.DE-FG02-03ER46097 and NIU Institute for Nanoscience, Engineering, and Technology. The work at Brookhaven was supported by the US Department of Energy, Division of Materials Science, under Contract No. DE-AC02-98CH10886. Work at Argonne National Laboratory and use of the Advanced Photon Source was supported by the US DOE, Office of Science, Office of Basic Energy Sciences, under Contract No. DE-AC02-06CH11357.

APPENDIX A: RIXS FORMULA DERIVATION

As explained in Sec. II A, we get the following formula from the Kramers-Heisenberg formula, Eq. (1), in the limit of completely localized core hole,

$$I(\omega,\mathbf{k},\mathbf{k}',\boldsymbol{\epsilon},\boldsymbol{\epsilon}') \propto \sum_f \left| \sum_{\mathbf{R}} \sum_{\mathbf{d}} \sum_{n^{\mathbf{R}+\mathbf{d}}} \frac{\langle f|\mathcal{D}'^{\dagger}|n^{\mathbf{R}+\mathbf{d}}\rangle\langle n^{\mathbf{R}+\mathbf{d}}|\mathcal{D}|g\rangle}{E_g+\hbar\omega_{\mathbf{k}}-E_{n^{\mathbf{d}}}+i\Gamma_{n^{\mathbf{d}}}} \right|^2 \times \delta(E_g-E_f+\hbar\omega), \tag{A1}$$

where $|n^{\mathbf{R}+\mathbf{d}}\rangle$ represents the intermediate energy eigenstate with the core hole at a site $\mathbf{R}+\mathbf{d}$ within the unit cell at a lattice point $\mathbf{R}$. Further applying the dipole approximation to the K-edge scattering amplitude, we obtain

$$\langle f|\mathcal{D}'^{\dagger}|n^{\mathbf{R}+\mathbf{d}}\rangle\langle n^{\mathbf{R}+\mathbf{d}}|\mathcal{D}|g\rangle = e^{-i(\mathbf{k}'-\mathbf{k})\cdot(\mathbf{R}+\mathbf{d})}\boldsymbol{\epsilon}'\cdot\langle f|\mathbf{r}|n^{\mathbf{R}+\mathbf{d}}\rangle\boldsymbol{\epsilon}\cdot\langle n^{\mathbf{R}+\mathbf{d}}|\mathbf{r}|g\rangle. \tag{A2}$$

Two many-body states $|\Psi^0\rangle$ and $|\Psi^{\mathbf{R}}\rangle$, which have total momentum $\hbar\boldsymbol{\kappa}$ and identical wave functions in two different coordinate systems with the coordinates for $|\Psi^{\mathbf{R}}\rangle$ shifted with respect to the coordinates for $|\Psi^0\rangle$ by $\mathbf{R}$, are related to each other by a phase factor $|\Psi^{\mathbf{R}}\rangle = e^{-i\boldsymbol{\kappa}\cdot\mathbf{R}}|\Psi^0\rangle$. Assuming that $|g\rangle$ and $|f\rangle$ have net momenta of zero and $\hbar\mathbf{k}_f$, respectively, we obtain the following relation [42]:

$$\langle f|\mathbf{r}|n^{\mathbf{R}+\mathbf{d}}\rangle = e^{-i\mathbf{k}_f\cdot\mathbf{R}}\langle f|\mathbf{r}|n^{\mathbf{d}}\rangle, \tag{A3}$$

$$\langle n^{\mathbf{R}+\mathbf{d}}|\mathbf{r}|g\rangle = \langle n^{\mathbf{d}}|\mathbf{r}|g\rangle. \tag{A4}$$

Therefore the sum over lattice vectors $\mathbf{R}$ for the combined factor of $e^{-i(\mathbf{k}'-\mathbf{k}+\mathbf{k}_f)\cdot\mathbf{R}}$ from Eqs. (A2)–(A4) leads to the conservation of the crystal momentum $\delta(\mathbf{k}'-\mathbf{k}+\mathbf{k}_f+\mathbf{K})$, where $\mathbf{K}$ represents the reciprocal lattice vectors. This results in the following expression for the RIXS intensity:

$$I(\omega,\mathbf{k},\mathbf{k}',\boldsymbol{\epsilon},\boldsymbol{\epsilon}') \propto \sum_{\mathbf{K}}\sum_f \left| \sum_{\mathbf{d}}\sum_{n^{\mathbf{d}}} \frac{e^{-i(\mathbf{k}'-\mathbf{k})\cdot\mathbf{d}}\,\boldsymbol{\epsilon}'\cdot\langle f|\mathbf{r}|n^{\mathbf{d}}\rangle\,\boldsymbol{\epsilon}\cdot\langle n^{\mathbf{d}}|\mathbf{r}|g\rangle}{E_g+\hbar\omega_{\mathbf{k}}-E_{n^{\mathbf{d}}}+i\Gamma_{n^{\mathbf{d}}}} \right|^2 \times \delta(E_f+\hbar\omega_{\mathbf{k}'}-E_g-\hbar\omega_{\mathbf{k}})\,\delta(\mathbf{k}_f+\mathbf{k}'-\mathbf{k}+\mathbf{K}). \tag{A5}$$

By further assuming special experimental setups in which the polarization vectors $\boldsymbol{\epsilon}'$ and $\boldsymbol{\epsilon}$ give rise to a constant factor, as mentioned in Sec. II A, and neglecting a constant factor from the dipole moment between $4p$ and $1s$ wave functions, we obtain Eq. (2) in Sec. II A.

APPENDIX B: EXPRESSION OF THE MATRIX ELEMENTS IN THE K-EDGE RIXS FORMULA IN TERMS OF EIGENSTATES IN THE PRESENCE AND ABSENCE OF CORE HOLE

In general, we transform $\hat{H}_{\rm d}$ and $\hat{H}_{{\rm total},\mathbf{i}_c}$ into the reciprocal space as follows:

$$\hat{H}_{\rm d} = \sum_{\mathbf{k},\mathbf{k}'}\sum_{\mathbf{K},\mathbf{K}'}\sum_{\xi,\xi'}\sum_{\sigma} H^{\rm d}_{\mathbf{k}+\mathbf{K},\xi,\mathbf{k}'+\mathbf{K}',\xi',\sigma}\, d^{\dagger}_{\mathbf{k}+\mathbf{K},\xi,\sigma} d_{\mathbf{k}'+\mathbf{K}',\xi',\sigma}, \tag{B1}$$

and

$$\hat{H}_{{\rm total},\mathbf{i}_c} = \sum_{\mathbf{k},\mathbf{k}'}\sum_{\mathbf{K},\mathbf{K}'}\sum_{\xi,\xi'}\sum_{\sigma} H^{{\rm total},\mathbf{i}_c}_{\mathbf{k}+\mathbf{K},\xi,\mathbf{k}'+\mathbf{K}',\xi',\sigma} \times d^{\dagger}_{\mathbf{k}+\mathbf{K},\xi,\sigma} d_{\mathbf{k}'+\mathbf{K}',\xi',\sigma}, \tag{B2}$$

where $\mathbf{k}$ and $\mathbf{k}'$ represent vectors within the first Brillouin zone $\Omega_{\rm 1BZ}$, $\mathbf{K}$ and $\mathbf{K}'$ the reciprocal lattice vectors within the extended "first Brillouin zone" $\Omega_{\rm ExZ}$ defined by the core hole site $\mathbf{i}$. Spin states are represented by σ, and orbital states by ξ and ξ'.

From the eigenstates $|l\mathbf{k}\sigma\rangle$ of $\hat{H}_{\rm d}$ with the wave vector $\mathbf{k} \in \Omega_{\rm 1BZ}$ within the lth lowest energy band, and the mth lowest energy eigenstate $|m\sigma\rangle$ of $\hat{H}_{\rm total,i_c}$, we define $\beta_{l\mathbf{k}m\sigma} = \langle l\mathbf{k}\sigma|m\sigma\rangle$. In the RIXS formula Eq. (3), $\langle n^{\mathbf{d}}_{\rm low}|\underline{s}^{\dagger}_{\mathbf{d}}|g\rangle$ and $\langle l_e\mathbf{k}_e l_h\mathbf{k}_h\sigma|\underline{s}_{\mathbf{d}}|n^{\mathbf{d}}_{\rm low}\rangle$ are found from

$$\langle n^{\mathbf{d}}_{\rm low}|\underline{s}^{\dagger}_{\mathbf{d}}|g\rangle = \prod_{\sigma=\uparrow\downarrow} \begin{vmatrix} \beta_{1\mathbf{k}_1 1\sigma} & \beta_{1\mathbf{k}_1 2\sigma} & \cdots & \beta_{1\mathbf{k}_1 \frac{N_e}{2}\sigma} \\ \beta_{1\mathbf{k}_2 1\sigma} & \beta_{1\mathbf{k}_2 2\sigma} & \cdots & \beta_{1\mathbf{k}_2 \frac{N_e}{2}\sigma} \\ \vdots & \vdots & \ddots & \vdots \\ \beta_{l_h^{\max}\mathbf{k}_{N_k} 1\sigma} & \beta_{l_h^{\max}\mathbf{k}_{N_k} 2\sigma} & \cdots & \beta_{l_h^{\max}\mathbf{k}_{N_k} \frac{N_e}{2}\sigma} \end{vmatrix}, \tag{B3}$$

$$\langle l_e\mathbf{k}_e l_h\mathbf{k}_h\sigma|\underline{s}_{\mathbf{d}}|n^{\mathbf{d}}_{\rm low}\rangle = \begin{vmatrix} \beta_{1\mathbf{k}_1 1\sigma} & \beta_{1\mathbf{k}_1 2\sigma} & \cdots & \beta_{1\mathbf{k}_1 \frac{N_e}{2}\sigma} \\ \beta_{1\mathbf{k}_2 1\sigma} & \beta_{1\mathbf{k}_2 2\sigma} & \cdots & \beta_{\sigma 1\mathbf{k}_2 \frac{N_e}{2}} \\ \vdots & \vdots & \ddots & \vdots \\ \beta_{l''_h\mathbf{k}''_h 1\sigma} & \beta_{l''_h\mathbf{k}''_h 2\sigma} & \cdots & \beta_{l''_h\mathbf{k}''_h \frac{N_e}{2}\sigma} \\ \beta_{l_e\mathbf{k}_e 1\sigma} & \beta_{l_e\mathbf{k}_e 2\sigma} & \cdots & \beta_{l_e\mathbf{k}_e \frac{N_e}{2}\sigma} \\ \beta_{l'''_h\mathbf{k}'''_h 1\sigma} & \beta_{l'''_h\mathbf{k}'''_h 2\sigma} & \cdots & \beta_{l'''_h\mathbf{k}'''_h \frac{N_e}{2}\sigma} \\ \vdots & \vdots & \ddots & \vdots \\ \beta_{l_h^{\max}\mathbf{k}_{N_k} 1\sigma} & \beta_{l_h^{\max}\mathbf{k}_{N_k} 2\sigma} & \cdots & \beta_{l_h^{\max}\mathbf{k}_{N_k} \frac{N_e}{2}\sigma} \end{vmatrix} \times \begin{vmatrix} \beta_{1\mathbf{k}_1 1\bar{\sigma}} & \beta_{1\mathbf{k}_1 2\bar{\sigma}} & \cdots & \beta_{1\mathbf{k}_1 \frac{N_e}{2}\bar{\sigma}} \\ \beta_{1\mathbf{k}_2 1\bar{\sigma}} & \beta_{1\mathbf{k}_2 2\bar{\sigma}} & \cdots & \beta_{1\mathbf{k}_2 \frac{N_e}{2}\bar{\sigma}} \\ \vdots & \vdots & \ddots & \vdots \\ \beta_{l_h^{\max}\mathbf{k}_{N_k} 1\bar{\sigma}} & \beta_{l_h^{\max}\mathbf{k}_{N_k} 2\bar{\sigma}} & \cdots & \beta_{l_h^{\max}\mathbf{k}_{N_k} \frac{N_e}{2}\bar{\sigma}} \end{vmatrix}, \tag{B4}$$

where N_e represents the total electron number, N_k is the number of $\mathbf{k}$ points in $\Omega_{\rm 1BZ}$, $l_h^{\max}$ is the index for the highest occupied band, and $\bar{\sigma} = -\sigma$. In Eq. (B4), the set of band and momentum indices, $(l''_h, \mathbf{k}''_h)$ and $(l'''_h, \mathbf{k}'''_h)$, represent the occupied states right before and right after the hole state represented by $(l_h, \mathbf{k}_h)$ when the eigenstates of $\hat{H}_{\rm d}$ are ordered according to the band index and momentum index [43].

APPENDIX C: EXPRESSIONS OF THE HAMILTONIANS IN RECIPROCAL SPACE WITH AND WITHOUT A 1*s* CORE HOLE FOR $La_{0.5}Sr_{1.5}MnO_4$

In the absence of the core hole, the Hamiltonian for a single layer of $La_{0.5}Sr_{1.5}MnO_4$ has the following form in reciprocal space:

$$\hat{H}_{\rm d} = \sum_{\sigma,\mathbf{k}\in\Omega_{\rm 1BZ}} d^{\dagger}_{\mathbf{k}\sigma}\left(H^{\rm d,nonint}_{\mathbf{k}\sigma} + H^{\rm dd,HF}_{\mathbf{k}\sigma}\right)d_{\mathbf{k}\sigma}, \tag{C1}$$

where

$$\begin{aligned} d^{\dagger}_{\mathbf{k}\sigma} = \big(&d^{\dagger}_{\mathbf{k}+\mathbf{K}_1,1,\sigma}, d^{\dagger}_{\mathbf{k}+\mathbf{K}_1,2,\sigma}, d^{\dagger}_{\mathbf{k}+\mathbf{K}_2,1,\sigma}, d^{\dagger}_{\mathbf{k}+\mathbf{K}_2,2,\sigma}, d^{\dagger}_{\mathbf{k}+\mathbf{K}_3,1,\sigma}, d^{\dagger}_{\mathbf{k}+\mathbf{K}_3,2,\sigma}, d^{\dagger}_{\mathbf{k}+\mathbf{K}_4,1,\sigma}, d^{\dagger}_{\mathbf{k}+\mathbf{K}_4,2,\sigma}, \\ &d^{\dagger}_{\mathbf{k}+\mathbf{K}_5,1,\sigma}, d^{\dagger}_{\mathbf{k}+\mathbf{K}_5,2,\sigma}, d^{\dagger}_{\mathbf{k}+\mathbf{K}_6,1,\sigma}, d^{\dagger}_{\mathbf{k}+\mathbf{K}_6,2,\sigma}, d^{\dagger}_{\mathbf{k}+\mathbf{K}_7,1,\sigma}, d^{\dagger}_{\mathbf{k}+\mathbf{K}_7,2,\sigma}, d^{\dagger}_{\mathbf{k}+\mathbf{K}_8,1,\sigma}, d^{\dagger}_{\mathbf{k}+\mathbf{K}_8,2,\sigma}\big) \end{aligned} \tag{C2}$$

with $\mathbf{K}_1$, $\mathbf{K}_2$, $\mathbf{K}_3$, $\mathbf{K}_4$, $\mathbf{K}_5$, $\mathbf{K}_6$, $\mathbf{K}_7$, and $\mathbf{K}_8$ representing (0,0), $(\frac{\pi}{a},0)$, $(0,\frac{\pi}{a})$, $(\frac{\pi}{a},\frac{\pi}{a})$, $(-\frac{\pi}{2a},-\frac{\pi}{2a})$, $(\frac{\pi}{2a},-\frac{\pi}{2a})$, $(-\frac{\pi}{2a},\frac{\pi}{2a})$, and $(\frac{\pi}{2a},\frac{\pi}{2a})$, respectively,

$$H^{\rm d,nonint}_{\mathbf{k}\sigma} = \begin{pmatrix} M_1+W_{3u} & -G_\sigma & G_\sigma & W_{1s}+W_{3s} & W_{2s} & G_\sigma & G_\sigma & W_{2s} \\ -G_\sigma & M_2+W_{3u} & W_{1s}+W_{3s} & G_\sigma & G_\sigma & W_{2s} & W_{2s} & G_\sigma \\ G_\sigma & W_{1s}+W_{3s} & M_3+W_{3u} & -G_\sigma & G_\sigma & W_{2s} & W_{2s} & G_\sigma \\ W_{1s}+W_{3s} & G_\sigma & -G_\sigma & M_4+W_{3u} & W_{2s} & G_\sigma & G_\sigma & W_{2s} \\ W_{2s} & G_\sigma & G_\sigma & W_{2s} & M_5+W_{3u} & -G_\sigma & G_\sigma & W_{1s}+W_{3s} \\ G_\sigma & W_{2s} & W_{2s} & G_\sigma & -G_\sigma & M_6+W_{3u} & W_{1s}+W_{3s} & G_\sigma \\ G_\sigma & W_{2s} & W_{2s} & G_\sigma & G_\sigma & W_{1s}+W_{3s} & M_7+W_{3u} & -G_\sigma \\ W_{2s} & G_\sigma & G_\sigma & W_{2s} & W_{1s}+W_{3s} & G_\sigma & -G_\sigma & M_8+W_{3u} \end{pmatrix}, \tag{C3}$$

$$M_j = \begin{pmatrix} -\frac{t_0}{2}[\cos(k_x+K_{j,x})+\cos(k_y+K_{j,y})] & \frac{\sqrt{3}t_0}{2}[\cos(k_x+K_{j,x})-\cos(k_y+K_{j,y})] \\ \frac{\sqrt{3}t_0}{2}[\cos(k_x+K_{j,x})-\cos(k_y+K_{j,y})] & -\frac{3t_0}{2}[\cos(k_x+K_{j,x})+\cos(k_y+K_{j,y})] \end{pmatrix}, \tag{C4}$$

$$G_{\uparrow} = \begin{pmatrix} -J_H S_c/2 & 0 \\ 0 & -J_H S_c/2 \end{pmatrix}, \tag{C5}$$

$$G_{\downarrow} = \begin{pmatrix} J_H S_c/2 & 0 \\ 0 & J_H S_c/2 \end{pmatrix}, \tag{C6}$$

$$W_{1s} = \begin{pmatrix} -\beta\lambda Q_{1s} & 0 \\ 0 & -\beta\lambda Q_{1s} \end{pmatrix}, \tag{C7}$$

$$W_{2s} = \begin{pmatrix} 0 & \lambda Q_{2s} \\ \lambda Q_{2s} & 0 \end{pmatrix}, \tag{C8}$$

$$W_{3u} = \begin{pmatrix} -\lambda Q_{3u} & 0 \\ 0 & \lambda Q_{3u} \end{pmatrix}, \tag{C9}$$

$$W_{3s} = \begin{pmatrix} -\lambda Q_{3s} & 0 \\ 0 & \lambda Q_{3s} \end{pmatrix}, \tag{C10}$$

$Q_{1s} = 0.053$ Å, $Q_{2s} = 0.054$ Å, $Q_{3u} = 0.107$ Å, and $Q_{3s} = -0.012$ Å (Ref. [32]). The element of the 16×16 matrix $H^{\mathrm{dd,HF}}_{\mathbf{k}\sigma}$ is independent of $\mathbf{k}$,

$$\left(H^{\mathrm{dd,HF}}_{\mathbf{k}\sigma}\right)_{2(j-1)+\xi,2(j'-1)+\xi'} = \sum_{\mathbf{i}_u,\eta} \frac{U_{\mathbf{i}_u\eta\sigma}}{8} e^{-i(\mathbf{K}_j-\mathbf{K}_{j'})\cdot\mathbf{i}_u} \left(R_{\mathbf{i}_u\eta}\right)_{\xi\xi'}, \tag{C11}$$

where $\eta = +,-$, $j,j' = 1,2,\ldots,8$, and $\xi,\xi' = 1,2$. Further, $\mathbf{i}_u$ represents the position of the Mn ions within the unit cell, that is, (0,0), $(a,0)$, $(2a,0)$, $(3a,0)$, $(a,-a)$, $(2a,-a)$, (a,a), and $(2a,a)$ in Fig. 3, and

$$R_{\mathbf{i}_u-} = \begin{pmatrix} \cos^2\theta_{\mathbf{i}_u} & \cos\theta_{\mathbf{i}_u}\sin\theta_{\mathbf{i}_u} \\ \cos\theta_{\mathbf{i}_u}\sin\theta_{\mathbf{i}_u} & \sin^2\theta_{\mathbf{i}_u} \end{pmatrix}, \tag{C12}$$

$$R_{\mathbf{i}_u+} = \begin{pmatrix} \sin^2\theta_{\mathbf{i}_u} & -\cos\theta_{\mathbf{i}_u}\sin\theta_{\mathbf{i}_u} \\ -\cos\theta_{\mathbf{i}_u}\sin\theta_{\mathbf{i}_u} & \cos^2\theta_{\mathbf{i}_u} \end{pmatrix}. \tag{C13}$$

$\theta_{\mathbf{i}}$ is defined from the local lower $(-)$ and upper $(+)$ Jahn-Teller eigenstates,

$$d^{\dagger}_{\mathbf{i}-\sigma} = d^{\dagger}_{\mathbf{i}1\sigma}\cos\theta_{\mathbf{i}} + d^{\dagger}_{\mathbf{i}2\sigma}\sin\theta_{\mathbf{i}}, \tag{C14}$$

$$d^{\dagger}_{\mathbf{i}+\sigma} = -d^{\dagger}_{\mathbf{i}1\sigma}\sin\theta_{\mathbf{i}} + d^{\dagger}_{\mathbf{i}2\sigma}\cos\theta_{\mathbf{i}}. \tag{C15}$$

At Mn^{3+} sites in the x/y directional legs of the zigzag chain in Fig. 3,

$$\tan\theta_{\mathbf{i}} = \pm\frac{Q_{3u}+Q_{3s}-\sqrt{(Q_{3u}+Q_{3s})^2+4Q_{2s}^2}}{2Q_{2s}}. \tag{C16}$$

At Mn^{4+} sites, $\theta_{\mathbf{i}} = 0$. The matrix for the number operator in reciprocal space is necessary to evaluate $U_{\mathbf{i}_u\eta\sigma}$ and its element is given below:

$$\left(n^{\mathbf{i}_u\eta\sigma}_{\mathbf{k}}\right)_{2(j-1)+\xi,2(j'-1)+\xi'} = e^{-i(\mathbf{K}_j-\mathbf{K}_{j'})\cdot\mathbf{i}_u}\left(R_{\mathbf{i}_u\eta}\right)_{\xi\xi'}. \tag{C17}$$

We find the eigenstates and eigenenergies of the 16×16 matrix $H^{\mathrm{d}}_{\mathbf{k}\sigma} = H^{\mathrm{d,nonint}}_{\mathbf{k}\sigma} + H^{\mathrm{dd,HF}}_{\mathbf{k}\sigma}$ at chosen set of $\mathbf{k}$ points through the Hartree-Fock iterative calculations, which are used to find the electronic DOS in the absence of the core hole shown in Figs. 5(a) and 6(a).

The Hamiltonian in the presence of the core hole at a site $\mathbf{i}_c$ for $N \times N$ cluster model of $La_{0.5}Sr_{1.5}MnO_4$, with N multiple of 4, is presented below:

$$\hat{H}_{\mathrm{total},\mathbf{i}_c} = \sum_{\sigma,\ \mathbf{k},\mathbf{k}'\in\Omega_{1\mathrm{BZ}}} d^{\dagger}_{\mathbf{k}\sigma}\left(H^{\mathrm{d,nonint}}_{\mathbf{k}\sigma}\delta_{\mathbf{k}\mathbf{k}'} + H^{\mathrm{dd,HF}}_{\mathbf{k}\mathbf{k}'\sigma} + H^{\mathrm{sd},\mathbf{i}_c}_{\mathbf{k}\mathbf{k}'\sigma}\right) d_{\mathbf{k}'\sigma}, \tag{C18}$$

where

$$\left(H^{\mathrm{dd,HF}}_{\mathbf{k}\mathbf{k}'\sigma}\right)_{2(j-1)+\xi,2(j'-1)+\xi'} = \sum_{\mathbf{i},\eta}\frac{U_{\mathbf{i}\eta\sigma}}{N^2}\, e^{-i(\mathbf{k}-\mathbf{k}')\cdot\mathbf{i}}\, e^{-i(\mathbf{K}_j-\mathbf{K}_{j'})\cdot\mathbf{i}}\left(R_{\mathbf{i}\eta}\right)_{\xi\xi'}, \tag{C19}$$

$$\left(H^{\mathrm{sd},\mathbf{i}_c}_{\mathbf{k}\mathbf{k}'\sigma}\right)_{2(j-1)+\xi,2(j'-1)+\xi'} = U_{\mathrm{core}}\, e^{-i(\mathbf{k}-\mathbf{k}')\cdot\mathbf{i}_c}\, e^{-i(\mathbf{K}_j-\mathbf{K}_{j'})\cdot\mathbf{i}_c}\,\delta_{\xi\xi'}, \tag{C20}$$

with $\eta = +,-$, $j,j' = 1,2,\ldots,8$, and $\xi,\xi' = 1,2$. For the evaluation of $U_{\mathbf{i}\eta\sigma}$, the number operator in reciprocal space is necessary, shown below:

$$\hat{n}^{\mathbf{i}\eta\sigma} = \sum_{\mathbf{k},\mathbf{k}'\in\Omega_{1\mathrm{BZ}}} d^{\dagger}_{\mathbf{k}\sigma}\, n^{\mathbf{i}\eta\sigma}_{\mathbf{k}\mathbf{k}'}\, d_{\mathbf{k}'\sigma}, \tag{C21}$$

where

$$\left(n^{\mathbf{i}\eta\sigma}_{\mathbf{k}\mathbf{k}'}\right)_{2(j-1)+\xi,2(j'-1)+\xi'} = e^{-i(\mathbf{k}-\mathbf{k}')\cdot\mathbf{i}}\, e^{-i(\mathbf{K}_j-\mathbf{K}_{j'})\cdot\mathbf{i}}(R_{\mathbf{i}\eta})_{\xi\xi'}. \tag{C22}$$

Eigenvectors and eigenvalues are found for the $2N^2 \times 2N^2$ matrix of $\hat{H}_{\mathrm{total},\mathbf{i}_c}$ for each spin direction σ in the presence of the core hole, through the Hartree-Fock iterative calculations. When necessary, the Pulay mixing method is used to reach a convergence [44,45]. The eigenstates and eigenenergies in the absence of the core hole for the same cluster are found by setting $U_{\mathrm{core}} = 0$ and repeating the Hartree-Fock iterative calculations. The two sets of eigenstates and eigenvalues give $\varepsilon_{l\mathbf{k}\sigma}$, $\varepsilon_{m\sigma}$, and $\beta_{l\mathbf{k}m\sigma}$, which are used for the K-edge RIXS spectrum calculations of $La_{0.5}Sr_{1.5}MnO_4$.

APPENDIX D: ELECTRON NUMBERS AT Mn^{3+} AND Mn^{4+} SITES

In this Appendix, we discuss the electron numbers on Mn ions. In our effective Hamiltonian, the state created by $d^{\dagger}_{\mathbf{i}\xi\sigma}$ is a hybridized state of atomic Mn $3d$ orbital and surrounding atomic O $2p$ orbitals. Therefore e_g electron numbers of 0.87 and 0.13 found for "Mn^{3+}" and "Mn^{4+}" sites in our effective Hamiltonian do not represent the actual numbers on Mn ions, which can be measured by resonant x-ray scattering. For a proper comparison, we carry out an analysis in terms of *atomic* Mn $3d$ and O $2p$ orbitals, similar to Ref. [46]. In the basis of $|d^4\rangle$ and $|d^5\underline{L}\rangle$, where d^n and $\underline{L}$ represent the presence of n electrons in atomic Mn $3d$ level and a hole in the ligand O $2p$ level of e_g symmetry, the Hamiltonian for the states with one e_g electron is

$$H_{\mathrm{one}\ e_g} = \begin{pmatrix} 0 & 2t_{\mathrm{dp}} \\ 2t_{\mathrm{dp}} & \Delta \end{pmatrix}, \tag{D1}$$

where t_{dp} represents the O $2p$ – Mn $3d$ electron hopping amplitude and Δ is the energy difference between Mn $3d$

and O $2p$ levels. Similarly, the Hamiltonian for the states with zero e_g electron is

$$H_{\text{zero } e_g} = \begin{pmatrix} 0 & 2t_{\text{dp}} \\ 2t_{\text{dp}} & \Delta - U_{\text{atomic}} \end{pmatrix}, \tag{D2}$$

in the basis of $|d^3\rangle$ and $|d^4\underline{L}\rangle$, where $3d$–$3d$ Coulomb interaction U_{atomic} is included to account for one less $3d$ electrons in $|d^4\underline{L}\rangle$ than in $|d^5\underline{L}\rangle$.

The lower-energy eigenstates of $H_{\text{one } e_g}$ and $H_{\text{zero } e_g}$,

$$|\text{one } e_g \text{ electron}\rangle = \mu_1|d^4\rangle + \nu_1|d^5\underline{L}\rangle, \tag{D3}$$

$$|\text{zero } e_g \text{ electron}\rangle = \mu_0|d^3\rangle + \nu_0|d^4\underline{L}\rangle, \tag{D4}$$

correspond to the states with one and zero electron in hybridized e_g levels considered in our effective Hamiltonian $\hat{H}_{\text{d}}$. Therefore $|\text{one } e_g \text{ electron}\rangle$ state has $4|\mu_1|^2 + 5|\nu_1|^2$ electrons in atomic Mn $3d$ levels, whereas $|\text{zero } e_g \text{ electron}\rangle$ state has $3|\mu_0|^2 + 4|\nu_0|^2$ electrons in atomic Mn $3d$ levels. Therefore n_{e_g} electrons in the hybridized e_g levels obtained from $\hat{H}_{\text{d}}$ corresponds to $n_{\text{atomic Mn}}$ electrons on the atomic Mn $3d$ levels, defined as

$$n_{\text{atomic Mn}} = n_{e_g}(4|\mu_1|^2 + 5|\nu_1|^2) + (1 - n_{e_g})(3|\mu_0|^2 + 4|\nu_0|^2). \tag{D5}$$

For typical values of $t_{\text{dp}} = 1$ eV, $\Delta = 4$ eV, $U_{\text{atomic}} = 7$ eV, and $n_{e_g} = 0.87$ and 0.13 obtained for e_g levels around "Mn^{3+}" and "Mn^{4+}" sites for $t_0 = 0.9$ eV case, we find $n_{\text{atomic Mn}} = 4.10$ and 3.84 for nominal Mn^{3+} and Mn^{4+} ions [35], and the difference is only about 0.26, which is much smaller than the difference of 0.74 between n_{e_g}'s and is consistent with 0.15–0.3 suggested by resonant x-ray scattering at the Mn K-edge and bond valance sum method [32,47].

[1] M. Z. Hasan, E. D. Isaacs, Z.-X. Shen, L. L. Miller, K. Tsutsui, T. Tohyama, and S. Maekawa, Science **288**, 1811 (2000).

[2] T. P. Devereaux, G. E. D. McCormack, and J. K. Freericks, Phys. Rev. Lett. **90**, 067402 (2003).

[3] K. Ishii, T. Inami, K. Ohwada, K. Kuzushita, J. Mizuki, Y. Murakami, S. Ishihara, Y. Endoh, S. Maekawa, K. Hirota, and Y. Moritomo, Phys. Rev. B **70**, 224437 (2004).

[4] S. Grenier, J. P. Hill, V. Kiryukhin, W. Ku, Y.-J. Kim, K. J. Thomas, S.-W. Cheong, Y. Tokura, Y. Tomioka, D. Casa, and T. Gog, Phys. Rev. Lett. **94**, 047203 (2005).

[5] R. S. Markiewicz and A. Bansil, Phys. Rev. Lett. **96**, 107005 (2006).

[6] M. Takahashi, J.-i. Igarashi, and T. Nomura, Phys. Rev. B **75**, 235113 (2007).

[7] T. A. Tyson, Q. Qian, M. A. DeLeon, C. Dubourdieu, L. Fratila, Y. Q. Cai, and K. H. Ahn, Appl. Phys. Lett. **90**, 101915 (2007).

[8] L. J. P. Ament, M. van Veenendaal, T. P. Devereaux, J. P. Hill, and J. van den Brink, Rev. Mod. Phys. **83**, 705 (2011).

[9] C.-C. Kao, W. A. L. Caliebe, J. B. Hastings, and J.-M. Gillet, Phys. Rev. B **54**, 16361 (1996).

[10] P. M. Platzman and E. D. Isaacs, Phys. Rev. B **57**, 11107 (1998).

[11] J. P. Hill, C.-C. Kao, W. A. L. Caliebe, M. Matsubara, A. Kotani, J. L. Peng, and R. L. Greene, Phys. Rev. Lett. **80**, 4967 (1998).

[12] P. Abbamonte, C. A. Burns, E. D. Isaacs, P. M. Platzman, L. L. Miller, S. W. Cheong, and M. V. Klein, Phys. Rev. Lett. **83**, 860 (1999).

[13] J. van den Brink and M. van Veenendaal, Europhys. Lett. **73**, 121 (2006).

[14] J. Kim, D. S. Ellis, H. Zhang, Y.-J. Kim, J. P. Hill, F. C. Chou, T. Gog, and D. Casa, Phys. Rev. B **79**, 094525 (2009).

[15] K. H. Ahn, A. J. Fedro, and M. van Veenendaal, Phys. Rev. B **79**, 045103 (2009).

[16] T. Semba, M. Takahashi, and J.-i. Igarashi, Phys. Rev. B **78**, 155111 (2008).

[17] Y. Moritomo, Y. Tomioka, A. Asamitsu, Y. Tokura, and Y. Matsui, Phys. Rev. B **51**, 3297 (1995).

[18] W. Bao, C. H. Chen, S. A. Carter, and S.-W. Cheong, Solid State Commun. **98**, 55 (1996).

[19] B. J. Sternlieb, J. P. Hill, U. C. Wildgruber, G. M. Luke, B. Nachumi, Y. Moritomo, and Y. Tokura, Phys. Rev. Lett. **76**, 2169 (1996).

[20] X. Liu, T. F. Seman, K. H. Ahn, M. van Veenendaal, D. Casa, D. Prabhakaran, A. T. Boothroyd, H. Ding, and J. P. Hill, Phys. Rev. B **87**, 201103(R) (2013).

[21] Y.-J. Kim, J. P. Hill, S. Wakimoto, R. J. Birgeneau, F. C. Chou, N. Motoyama, K. M. Kojima, S. Uchida, D. Casa, and T. Gog, Phys. Rev. B **76**, 155116 (2007).

[22] http://web.njit.edu/~kenahn/programs.htm

[23] H. A. Kramers and W. Heisenberg, Z. Phys. **31**, 681 (1925).

[24] L. C. Davis and L. A. Feldkamp, J. Appl. Phys. **50**, 1944 (1979).

[25] L. A. Feldkamp and L. C. Davis, Phys. Rev. B **22**, 4994 (1980).

[26] T. Ishikawa, K. Ookura, and Y. Tokura, Phys. Rev. B **59**, 8367 (1999).

[27] J. H. Jung, J. S. Ahn, J. Yu, T. W. Noh, J. Lee, Y. Moritomo, I. Solovyev, and K. Terakura, Phys. Rev. B **61**, 6902 (2000).

[28] J. Herrero-Martín, J. García, G. Subías, J. Blasco, and M. Concepción Sánchez, Phys. Rev. B **70**, 024408 (2004).

[29] L. Brey, Phys. Rev. Lett. **92**, 127202 (2004).

[30] M. Coey, Nature (London) **430**, 155 (2004).

[31] K. H. Ahn and A. J. Millis, Phys. Rev. B **61**, 13545 (2000).

[32] J. Herrero-Martín, J. Blasco, J. García, G. Subías, and C. Mazzoli, Phys. Rev. B **83**, 184101 (2011).

[33] We note that unlike the three-dimensional manganites, the degeneracy of the e_g levels are broken even without the Q_2 or Q_3 distortions because of the layered crystal structure. So, we should consider $\hat{H}_{\text{JT}}$ as the effective Hamiltonian that includes not only the effect of the oxygen octahedron but also the crystal field of farther ions.

[34] A. J. Millis, Phys. Rev. B **53**, 8434 (1996); K. H. Ahn and A. J. Millis, *ibid.* **58**, 3697 (1998).

[35] J. Herrero-Martín, A. Mirone, J. Fernández-Rodríguez, P. Glatzel, J. García, J. Blasco, and J. Geck, Phys. Rev. B **82**, 075112 (2010).

[36] L. J. Zeng, C. Ma, H. X. Yang, R. J. Xiao, J. Q. Li, and J. Jansen, Phys. Rev. B **77**, 024107 (2008).

[37] The e_g electron numbers in the absence of the core hole are 0.65 at the nominal Mn^{3+} site and 0.35 at the nominal Mn^{4+} site for $t_0 = 1.5$ eV case.

[38] F. Weber, S. Rosenkranz, J.-P. Castellan, R. Osborn, J. F. Mitchell, H. Zheng, D. Casa, J. H. Kim, and T. Gog, Phys. Rev. B **82**, 085105 (2010).

[39] We also note that the Fourier transform of electron number change shown in Figs. 7(a) and 7(b) has a maximum at $(\pm\frac{\pi}{a}, \pm\frac{\pi}{a})$, consistent with the point in reciprocal space with maximum integrated RIXS intensity. However, such correspondence does not apply to $t_0 = 1.5$ eV case, indicating further study is required to establish the exact relation between RIXS intensities in reciprocal space and screening in real space.

[40] The periodicity visible in Fig. 13 with respect to $\mathbf{b_1}/2$ and $\mathbf{b_2}/2$ does not correspond to charge, spin, or orbital ordering in CE-phase $La_{0.5}Sr_{1.5}MnO_4$. Complete understanding of such periodicity is left for future studies.

[41] D. Pines and P. Nozières, *The Theory of Quantum Liquids* (Perseus Books, Reading, Massachusetts, 1988), Vol. I, Chapter 2.

[42] We use the relation $\langle f|\mathbf{R}|n^{\mathbf{R}+\mathbf{d}}\rangle = \langle n^{\mathbf{R}+\mathbf{d}}|\mathbf{R}|g\rangle = 0$.

[43] In other words, from the $N_e/2 \times N_e/2$ part of the matrix of $\beta_{l\mathbf{k}m\sigma}$ with $m = 1, \ldots, N_e/2$ and $\varepsilon_{l\mathbf{k}\sigma} < \varepsilon_{\mathrm{F}}$, the row corresponding to $\mathbf{k} = \mathbf{k}_h$ and $l = l_h$ is replaced by the row corresponding to $\mathbf{k} = \mathbf{k}_e$ and $l = l_e$ in the matrix of $\beta_{l\mathbf{k}m\sigma}$.

[44] P. Pulay, Chem. Phys. Lett. **73**, 393 (1980).

[45] P. Pulay and R. F. Liu, J. Phys. Chem. **94**, 5548 (1990).

[46] M. A. van Veenendaal, H. Eskes, and G. A. Sawatzky, Phys. Rev. B **47**, 11462 (1993).

[47] N. E. Brese and M. O'Keeffe, Acta Crystallogr. Sect. B: Struct. Sci. **47**, 192 (1991); I. D. Brown, *ibid.* **48**, 553 (1992).